

Multi-wavelength study of the galactic PeVatron candidate LHAASO J2108+5157

S. Abe¹ A. Aguasca-Cabot² I. Agudo³ N. Alvarez Crespo⁴ L. A. Antonelli⁵
 C. Aramo⁶ A. Arbet-Engels⁷ M. Artero⁸ K. Asano¹ P. Aubert⁹ A. Baktash¹⁰
 A. Bamba¹¹ A. Baquero Larriva¹² L. Baroncelli¹³ U. Barres de Almeida¹⁴
 J. A. Barrio¹² I. Batkovic¹⁵ J. Baxter¹ J. Becerra González¹⁶ E. Bernardini¹⁵
 M. I. Bernardos³ J. Bernete Medrano¹⁷ A. Berti⁷ P. Bhattacharjee⁹
 N. Biederbeck¹⁸ C. Bigongiari⁵ E. Bissaldi¹⁹ O. Blanch⁸ P. Bordas²
 C. Buisson⁹ A. Bulgarelli¹³ I. Burelli²⁰ M. Buscemi²¹ M. Cardillo²²
 S. Caroff⁹ A. Carosi⁵ F. Cassol²³ D. Cauz²⁰ G. Ceribella¹ Y. Chai⁷
 K. Cheng¹ A. Chiavassa²⁴ M. Chikawa¹ L. Chytka²⁵ A. Cifuentes¹⁷
 J. L. Contreras¹² J. Cortina¹⁷ H. Costantini²³ G. D'Amico²⁶ M. Dalchenko²⁷
 A. De Angelis¹⁵ M. de Bony de Lavergne⁹ B. De Lotto²⁰ R. de Menezes²⁴
 G. Deleglise⁹ C. Delgado¹⁷ J. Delgado Mengual²⁸ D. della Volpe²⁷ M. Dellaiera⁹
 A. Di Piano¹³ F. Di Pierro²⁴ R. Di Tria²⁹ L. Di Venere²⁹ C. Díaz¹⁷
 R. M. Dominik¹⁸ D. Dominis Prester³⁰ A. Donini⁸ D. Dorner³¹ M. Doro¹⁵
 D. Elsässer¹⁸ G. Emery²⁷ J. Escudero³ V. Fallah Ramazani³² G. Ferrara²¹
 A. Fiasson^{9,33} L. Freixas Coromina¹⁷ S. Fröse¹⁸ S. Fukami¹ Y. Fukazawa³⁴
 E. Garcia⁹ R. Garcia López¹⁶ D. Gasparrini³⁵ D. Geyer¹⁸ J. Giesbrecht Paiva¹⁴
 N. Giglietto¹⁹ F. Giordano²⁹ E. Giro¹⁵ P. Gliwny³⁶ N. Godinovic³⁷ R. Grau⁸
 D. Green⁷ J. Green⁷ S. Gunji³⁸ J. Hackfeld³² D. Hadasch¹ A. Hahn⁷
 K. Hashiyama¹ T. Hassan¹⁷ K. Hayashi³⁹ L. Heckmann⁷ M. Heller²⁷
 J. Herrera Llorente¹⁶ K. Hirotani¹ D. Hoffmann²³ D. Horns¹⁰ J. Houles²³
 M. Hrabovsky²⁵ D. Hrupec⁴⁰ D. Hui¹ M. Hütten¹ R. Imazawa³⁴ T. Inada¹
 Y. Inome¹ K. Ioka⁴¹ M. Iori⁴² K. Ishio³⁶ Y. Iwamura¹ M. Jacquemont⁹
 I. Jimenez Martinez¹⁷ J. Jurysek^{43*} M. Kagaya¹ V. Karas⁴⁴ H. Katagiri⁴⁵
 J. Kataoka⁴⁶ D. Kerszberg⁸ Y. Kobayashi¹ A. Kong¹ H. Kubo¹ J. Kushida⁴⁷
 M. Lainez¹² G. Lamanna⁹ A. Lamastra⁵ T. Le Flour⁹ M. Linhoff¹⁸
 F. Longo⁴⁸ R. López-Coto³ M. López-Moya¹² A. López-Oramas¹⁶
 S. Loporchio²⁹ A. Lorini⁴⁹ P. L. Luque-Escamilla⁵⁰ P. Majumdar^{1,51}
 M. Makariev⁵² D. Mandat⁵³ M. Manganaro³⁰ G. Manicò²¹ K. Mannheim³¹
 M. Mariotti¹⁵ P. Marquez⁸ G. Marsella^{21,54} J. Martí⁵⁰ O. Martinez⁴
 G. Martínez¹⁷ M. Martínez⁸ P. Marusevec⁵⁵ A. Mas-Aguilar¹² G. Maurin⁹
 D. Mazin^{1,7} E. Mestre Guillen⁵⁶ S. Micanovic³⁰ D. Miceli¹⁵ T. Miener¹²
 J. M. Miranda⁴ R. Mirzoyan⁷ T. Mizuno⁵⁷ M. Molero Gonzalez¹⁶ E. Molina²
 T. Montaruli²⁷ I. Monteiro⁹ A. Moralejo⁸ D. Morcuende¹² A. Morselli³⁵
 K. Mrakovicic³⁰ K. Murase¹ A. Nagai²⁷ T. Nakamori³⁸ L. Nickel¹⁸

M. Nievas ¹⁶	K. Nishijima ⁴⁷	K. Noda ¹	D. Nosek ⁵⁸	S. Nozaki ⁷	M. Ohishi ¹
Y. Ohtani ¹	N. Okazaki ¹	A. Okumura ^{59,60}	R. Orito ⁶¹	J. Otero-Santos ¹⁶	
M. Palatiello ²⁰	D. Paneque ⁷	F. R. Pantaleo ¹⁹	R. Paoletti ⁴⁹	J. M. Paredes ²	
L. Pavletić ³⁰	M. Pech ⁵³	M. Pecimotika ³⁰	E. Pietropaolo ⁶²	G. Pirola ⁷	
F. Podobnik ⁴⁹	V. Poireau ⁹	M. Polo ¹⁷	E. Pons ⁹	E. Prandini ¹⁵	J. Prast ⁹
C. Priyadarshi ⁸	M. Prouza ⁵³	R. Rando ¹⁵	W. Rhode ¹⁸	M. Ribó ²	V. Rizi ⁶²
G. Rodriguez Fernandez ³⁵	T. Saito ¹	S. Sakurai ¹	D. A. Sanchez ⁹	T. Šarić ³⁷	
F. G. Saturni ⁵	J. Scherpenberg ⁷	B. Schleicher ³¹	F. Schmuckermair ⁷		
J. L. Schubert ¹⁸	F. Schussler ⁶³	T. Schweizer ⁷	M. Seglar Arroyo ⁹	J. Sitarek ³⁶	
V. Sliusar ⁴³	A. Spolon ¹⁵	J. Strišković ⁴⁰	M. Strzys ¹	Y. Suda ³⁴	Y. Sunada ⁶⁴
H. Tajima ⁵⁹	M. Takahashi ¹	H. Takahashi ³⁴	J. Takata ¹	R. Takeishi ¹	
P. H. T. Tam ¹	S. J. Tanaka ⁶⁵	D. Tateishi ⁶⁴	P. Temnikov ⁵²	Y. Terada ⁶⁴	
K. Terauchi ⁶⁶	T. Terzic ³⁰	M. Teshima ^{1,7}	M. Tluczykont ¹⁰	F. Tokanai ³⁸	
D. F. Torres ⁵⁶	P. Travnicek ⁵³	S. Truzzi ⁴⁹	A. Tutone ⁵	G. Uhrlrich ²⁷	
M. Vacula ²⁵	M. Vázquez Acosta ¹⁶	V. Verguilov ⁵²	I. Viale ¹⁵	A. Vigliano ²⁰	
C. F. Vigorito ^{24,67}	V. Vitale ³⁵	G. Voutsinas ²⁷	I. Vovk ¹	T. Vuillaume ⁹	
R. Walter ⁴³	M. Will ⁷	T. Yamamoto ⁶⁸	R. Yamazaki ⁶⁵	T. Yoshida ⁴⁵	
T. Yoshikoshi ¹	N. Zywucka ³⁶ (CTA-LST Project)		M. Balbo ⁴³	D. Eckert ⁴³	
		A. Tramacere ⁴³			

¹Institute for Cosmic Ray Research, University of Tokyo, 5-1-5, Kashiwa-no-ha, Kashiwa, Chiba 277-8582, Japan ; ²Departament de Física Quàntica i Astrofísica, Institut de Ciències del Cosmos, Universitat de Barcelona, IEEC-UB, Martí i Franquès, 1, 08028, Barcelona, Spain ; ³Instituto de Astrofísica de Andalucía-CSIC, Glorieta de la Astronomía s/n, 18008, Granada, Spain ; ⁴Grupo de Electronica, Universidad Complutense de Madrid, Av. Complutense s/n, 28040 Madrid, Spain ;

⁵INAF - Osservatorio Astronomico di Roma, Via di Frascati 33, 00040, Monteporzio Catone, Italy ; ⁶INFN Sezione di Napoli, Via Cintia, ed. G, 80126 Napoli, Italy ; ⁷Max-Planck-Institut für Physik, Föhringer Ring 6, 80805 München, Germany ; ⁸Institut de Fisica d'Altes Energies (IFAE), The Barcelona Institute of Science and Technology, Campus UAB, 08193 Bellaterra (Barcelona), Spain ;

⁹Univ. Savoie Mont Blanc, CNRS, Laboratoire d'Annecy de Physique des Particules - IN2P3, 74000 Annecy, France ; ¹⁰Universität Hamburg, Institut für Experimentalphysik, Luruper Chaussee 149, 22761 Hamburg, Germany ; ¹¹Graduate School of Science, University of Tokyo, 7-3-1 Hongo, Bunkyo-ku, Tokyo 113-0033, Japan ; ¹²EMFTEL department and IPARCOS, Universidad Complutense de Madrid, 28040 Madrid, Spain ; ¹³INAF - Osservatorio di Astrofisica e Scienza dello spazio di Bologna, Via Piero Gobetti 93/3, 40129 Bologna, Italy ; ¹⁴Centro Brasileiro de Pesquisas Físicas, Rua Xavier Sigaud 150, RJ 22290-180, Rio de Janeiro, Brazil ; ¹⁵INFN Sezione di Padova and Università degli Studi di Padova, Via Marzolo 8, 35131 Padova, Italy ; ¹⁶Instituto de Astrofísica de Canarias and Departamento de Astrofísica, Universidad de La Laguna, La Laguna, Tenerife, Spain ; ¹⁷CIEMAT, Avda. Complutense 40, 28040 Madrid, Spain ; ¹⁸Department of Physics, TU Dortmund University, Otto-Hahn-Str. 4, 44227 Dortmund, Germany ; ¹⁹INFN Sezione di Bari and Politecnico di Bari, via Orabona 4, 70124 Bari, Italy ; ²⁰INFN Sezione di Trieste and Università degli studi di Udine, via delle scienze 206, 33100 Udine, Italy. ; ²¹INFN Sezione di Catania, Via S. Sofia 64, 95123 Catania, Italy ; ²²INAF - Istituto di Astrofisica e Planetologia Spaziali (IAPS), Via del Fosso del Cavaliere 100, 00133 Roma, Italy ; ²³Aix Marseille Univ, CNRS/IN2P3, CPPM, Marseille, France ; ²⁴INFN Sezione di Torino, Via P. Giuria 1, 10125 Torino, Italy ; ²⁵Palacky

University Olomouc, Faculty of Science, 17. listopadu 1192/12, 771 46 Olomouc, Czech Republic ;
²⁶Department of Physics and Technology, University of Bergen, Museplass 1, 5007 Bergen, Norway ;
²⁷University of Geneva - Département de physique nucléaire et corpusculaire, 24 Quai Ernest
Ansernet, 1211 Genève 4, Switzerland ;²⁸Port d'Informació Científica, Edifici D, Carrer de
l'Albareda, 08193 Bellaterra (Cerdanyola del Vallès), Spain ;²⁹INFN Sezione di Bari and
Università di Bari, via Orabona 4, 70126 Bari, Italy ;³⁰University of Rijeka, Department of Physics,
Radmile Matejcic 2, 51000 Rijeka, Croatia ;³¹Institute for Theoretical Physics and Astrophysics,
Universität Würzburg, Campus Hubland Nord, Emil-Fischer-Str. 31, 97074 Würzburg, Germany ;
³²Institut für Theoretische Physik, Lehrstuhl IV: Plasma-Astroteilchenphysik, Ruhr-Universität
Bochum, Universitätsstraße 150, 44801 Bochum, Germany ;³³ILANCE, CNRS - University of
Tokyo International Research Laboratory, Kashiwa, Chiba 277-8582, Japan ;³⁴Physics Program,
Graduate School of Advanced Science and Engineering, Hiroshima University, 739-8526 Hiroshima,
Japan ;³⁵INFN Sezione di Roma Tor Vergata, Via della Ricerca Scientifica 1, 00133 Rome, Italy ;
³⁶Faculty of Physics and Applied Informatics, University of Lodz, ul. Pomorska 149-153, 90-236
Lodz, Poland ;³⁷University of Split, FESB, R. Boškovića 32, 21000 Split, Croatia ;³⁸Department of
Physics, Yamagata University, Yamagata 990-8560, Japan ;³⁹Tohoku University,
Astronomical Institute, Aobaku, Sendai 980-8578, Japan ;⁴⁰Josip Juraj Strossmayer University of
Osijek, Department of Physics, Trg Ljudevita Gaja 6, 31000 Osijek, Croatia ;⁴¹Kitashirakawa
Oiwakecho, Sakyo Ward, Kyoto, 606-8502, Japan ;⁴²INFN Sezione di Roma La Sapienza, P.le Aldo
Moro, 2 - 00185 Rome, Italy ;⁴³Department of Astronomy, University of Geneva, Chemin d'Ecogia
16, CH-1290 Versoix, Switzerland ;⁴⁴Astronomical Institute of the Czech Academy of Sciences,
Bocni II 1401 - 14100 Prague, Czech Republic ;⁴⁵Faculty of Science, Ibaraki University, Mito,
Ibaraki, 310-8512, Japan ;⁴⁶Faculty of Science and Engineering, Waseda University, Shinjuku,
Tokyo 169-8555, Japan ;⁴⁷Department of Physics, Tokai University, 4-1-1, Kita-Kaname, Hiratsuka,
Kanagawa 259-1292, Japan ;⁴⁸INFN Sezione di Trieste and Università degli Studi di Trieste, Via
Valerio 2 I, 34127 Trieste, Italy ;⁴⁹INFN and Università degli Studi di Siena, Dipartimento di
Scienze Fisiche, della Terra e dell'Ambiente (DSFTA), Sezione di Fisica, Via Roma 56, 53100
Siena, Italy ;⁵⁰Escuela Politécnica Superior de Jaén, Universidad de Jaén, Campus Las Lagunillas
s/n, Edif. A3, 23071 Jaén, Spain ;⁵¹Saha Institute of Nuclear Physics, Bidhannagar, Kolkata-700
064, India ;⁵²Institute for Nuclear Research and Nuclear Energy, Bulgarian Academy of Sciences,
72 boul. Tsarigradsko chaussee, 1784 Sofia, Bulgaria ;⁵³FZU - Institute of Physics of the Czech
Academy of Sciences, Na Slovance 1999/2, 182 21 Praha 8, Czech Republic ;⁵⁴Dipartimento di
Fisica e Chimica 'E. Segrè' Università degli Studi di Palermo, via delle Scienze, 90128 Palermo ;
⁵⁵Department of Applied Physics, University of Zagreb, Horvatovac 102a, 10000 Zagreb, Croatia ;
⁵⁶Institute of Space Sciences (ICE, CSIC), and Institut d'Estudis Espacials de Catalunya (IEEC), and
Institució Catalana de Recerca i Estudis Avançats (ICREA), Campus UAB, Carrer de Can Magrans,
s/n 08193 Bellaterra, Spain ;⁵⁷Hiroshima Astrophysical Science Center, Hiroshima University,
Higashi-Hiroshima, Hiroshima 739-8526, Japan ;⁵⁸Charles University, Institute of Particle and
Nuclear Physics, V Holešovičkách 2, 180 00 Prague 8, Czech Republic ;⁵⁹Institute for Space-Earth
Environmental Research, Nagoya University, Chikusa-ku, Nagoya 464-8601, Japan ;
⁶⁰Kobayashi-Maskawa Institute (KMI) for the Origin of Particles and the Universe, Nagoya
University, Chikusa-ku, Nagoya 464-8602, Japan ;⁶¹Graduate School of Technology, Industrial and
Social Sciences, Tokushima University, Tokushima 770-8506, Japan ;⁶²INFN Dipartimento di
Scienze Fisiche e Chimiche - Università degli Studi dell'Aquila and Gran Sasso Science Institute,
Via Vetoio 1, Viale Crispi 7, 67100 L'Aquila, Italy ;⁶³IRFU, CEA, Université Paris-Saclay, Bât 141,
91191 Gif-sur-Yvette, France ;⁶⁴Graduate School of Science and Engineering, Saitama University,
255 Simo-Ohkubo, Sakura-ku, Saitama city, Saitama 338-8570, Japan ;⁶⁵Department of Physical
Sciences, Aoyama Gakuin University, Fuchinobe, Sagamihara, Kanagawa, 252-5258, Japan ;
⁶⁶Division of Physics and Astronomy, Graduate School of Science, Kyoto University, Sakyo-ku,
Kyoto, 606-8502, Japan ;⁶⁷Dipartimento di Fisica - Università degli Studi di Torino, Via Pietro
Giuria 1 - 10125 Torino, Italy ;⁶⁸Department of Physics, Konan University, Kobe, Hyogo, 658-8501,
Japan; (October 12, 2022)

Abstract

Context: Several new Ultra-High-Energy (UHE) gamma-ray sources have recently been discovered by the LHAASO collaboration, which represent a step forward in the search for the so-called galactic PeVatrons, the enigmatic sources of the Galactic cosmic rays up to PeV energies. However, it has been shown that multi-TeV gamma-ray emission does not necessarily prove the existence of a hadronic accelerator in the source, in fact it could also be explained as inverse Compton scattering from electrons in a radiation dominated environment. A clear distinction between the two major emission mechanisms would only be possible taking into account multi-wavelength data and detailed morphology of the source.

Aims: We aim for understanding the nature of the unidentified source LHAASO J2108+5157, which is one of the few known UHE sources with no Very-High-Energy (VHE) counterpart.

Methods: We observed LHAASO J2108+5157 in the X-ray band with *XMM-Newton* in 2021 for a total of 3.8 hours and at TeV energies with the Large-Sized Telescope prototype (LST-1), yielding 49 hours of good quality data. In addition, we analyzed 12 years of *Fermi*-LAT data, to better constrain emission of its High-Energy (HE) counterpart 4FGL J2108.0+5155. We used *naima* and *jetset* software packages to examine leptonic and hadronic scenario of the multi-wavelength emission of the source.

Results: We found an excess (3.7σ) in the LST-1 data at energies $E > 3$ TeV. Further analysis in the whole LST-1 energy range assuming a point-like source, resulted in a hint (2.2σ) of hard emission which can be described with a single power law with photon index $\Gamma = 1.6 \pm 0.2$ between $0.3 - 100$ TeV. We did not find any significant extended emission which could be related to a Supernova Remnant (SNR) or Pulsar Wind Nebula (PWN) in the *XMM-Newton* data, which puts strong constraints on possible synchrotron emission of relativistic electrons. We revealed a new potential hard source in *Fermi*-LAT data with a significance of 4σ and photon index $\Gamma = 1.9 \pm 0.2$, which is not spatially correlated with LHAASO J2108+5157, but including it in the source model we were able to improve spectral representation of the HE counterpart 4FGL J2108.0+5155.

Conclusions: The LST-1 and LHAASO observations can be explained as inverse Compton dominated leptonic emission of relativistic electrons with cutoff energy of 100_{-30}^{+70} TeV. The low magnetic field in the source imposed by the X-ray upper limits on synchrotron emission is compatible with a hypothesis of a TeV halo. Furthermore, the spectral properties of the HE counterpart are consistent with a hypothesis of Geminga-like pulsar, which would be able to power the VHE-UHE emission. LST-1 and *Fermi*-LAT upper limits impose strong constraints on hadronic scenario of π^0 decay dominated emission from accelerated protons interacting with one of the two known molecular clouds in the direction of the UHE gamma-ray source, requiring hard spectral index, which is incompatible with the standard diffusive acceleration scenario. However, stochastic acceleration of protons in molecular clouds with turbulent magnetic field, or interaction of accelerated protons with gas clumps present in a SNR shell cannot be ruled out.

Key words. radiation mechanisms: non-thermal / gamma rays: general / pulsars: general / ISM: individual objects: LHAASO J2108+5157

1 Introduction

Cosmic rays (CR) with energies up to the knee (~ 1 PeV) are believed to be produced in hadronic PeVatrons, cosmic accelerators located in our Galaxy (for a review see e.g. Gabici et al. 2019). Despite substantial observational efforts in the latest decade, the origin of the highest energy galactic CRs remains unknown, mainly due to complicated reconstruction of direction of their origin, as they are subject to deflection in the Galactic magnetic field. When accelerated protons interact with ambient matter, they emit gamma rays through π^0 decay. Similarly electrons and positrons produce gamma rays via inverse Compton (IC) scattering on low energy photon fields, via bremsstrahlung when colliding with atomic nuclei of ambient matter, or via synchrotron radiation when interacting with magnetic fields. Studying Very-High-Energy (VHE, $0.1 < E < 100$ TeV) and Ultra-High-Energy (UHE, $E > 0.1$ PeV) cosmic gamma rays and disentangling different origins of the radiation thus plays an essential role in the search for cosmic PeVatrons (CTA Consortium et al. 2019, CTA Consortium, in prep.).

Diffusive shock acceleration (DSA) (Bell 1978) taking place in Supernova Remnants (SNRs) and Pulsar Wind Nebulae (PWNe) has been proposed as a possible mechanism to accelerate CR (Bell 2013). In several SNRs, a characteristic "pion-decay bump" spectral feature has been detected, providing evidence that proton acceleration takes place in these sources (Ackermann et al. 2013; Jogler & Funk 2016; H. E. S. S. Collaboration

*Corresponding authors: lst-contact@cta-observatory.org, Jakub.Jurysek@unige.ch, Matteo.Balbo@unige.ch, Roland.Walter@unige.ch, Dominique.Eckert@unige.ch, Andrea.Tramacere@unige.ch

et al. 2018b; Ambrogi et al. 2019; Abdollahi et al. 2022). However, none of the gamma-ray spectra of sources firmly identified as SNRs extends beyond 100 TeV (Aharonian et al. 2019; Zeng et al. 2019), which suggests that these sources are probably not capable of proton acceleration up to PeV energies.

The search for PeVatrons continues, and in the last few years several new candidates showing gamma-ray emission above 100 TeV have been discovered by Tibet AS γ collaboration (Amenomori et al. 2019; Tibet AS γ Collaboration et al. 2021) and HAWC collaboration (HAWC Collaboration et al. 2019). Recently, the LHAASO collaboration exploiting an unpreceded sensitivity of the LHAASO-KM2A instrument in the UHE range, reported the discovery of 12 UHE gamma-ray sources reaching energies up to 1.4 PeV (Cao et al. 2021b). Among these, there is only one unidentified source, with not yet detected TeV counterpart – LHAASO J2108+5157.

LHAASO J2108+5157 is the first gamma-ray source directly discovered in the UHE band, detected with a post-trial significance of 6.4σ above 100 TeV (Cao et al. 2021a). The position of the source is R.A. = $317.22^\circ \pm 0.07^\circ$, Dec = $51.95^\circ \pm 0.05^\circ$. The source is reported to be point-like with a 95% confidence level upper limit on its extension of 0.26° with a two-dimensional symmetrical Gaussian shape assumption. The spectrum of LHAASO J2108+5157 above 25 TeV can be described by a single power law with photon index of 2.83 ± 0.18 . There is no VHE or X-ray counterpart to the source, but Cao et al. (2021a) identified a close High-Energy (HE) point source 4FGL J2108.0+5155 (Abdollahi et al. 2020) at an angular distance of 0.13° . A dedicated analysis suggested that the HE source might be spatially extended (4FGL J2108.0+5155e) with extension of 0.48° . Its spectrum could be described as a single power law with a photon index 2.3 between 1 GeV and 1 TeV. The physical connection between Spectral Energy Distributions (SEDs) of the HE and UHE source is however not obvious due to very different spectral indices. Cao et al. (2021a) found the source to be coincident with the position of a molecular cloud [MML2017]4607 (Miville-Deschénes et al. 2017), which would support hypothesis of the hadronic origin of the emission, if CR protons collide with the ambient gas. The authors suggested that the extended emission of 4FGL J2108.0+5155e can be related to an old SNR, while the point-like UHE emission can be due to interaction of the escaping CRs from the SNR with the molecular cloud. Alternatively, they proposed that the relativistic CRs can be accelerated in one of the nearby open stellar clusters, but confirmation of such hypotheses is complicated due to an unknown distance of the source. A leptohadronic emission scenario was also proposed by Kar & Gupta (2022), where shock-accelerated electrons and protons were injected in the molecular cloud several thousand years ago during an explosion.

TeV halos in the vicinity of pulsars have been recently established as a class of extended VHE sources (Linden et al. 2017; Abeysekara et al. 2017; López-Coto et al. 2022), featuring bright TeV emission and hard spectrum (Sudoh et al. 2019). Gamma-ray emission in such sources can be produced in IC scattering of ambient photons by VHE electrons and positrons accelerated by the pulsar wind termination shock (Sudoh et al. 2019). Even though IC gamma-ray emission beyond 100 TeV is suppressed due to Klein-Nishina effect, it has been shown that IC can still dominate UHE emission in radiation dominated environments (e.g. Vannoni et al. 2009; Breuhaus et al. 2021). This mechanism was used to explain UHE gamma-ray emission of extended sources detected by HAWC, and three LHAASO sources associated with pulsars (Breuhaus et al. 2021, 2022). In addition, the study of Albert et al. (2021) suggests that UHE gamma-ray emission may be a generic feature in the vicinity of pulsars with high spin-down powers $\dot{E} > 10^{36}$ ergs $^{-1}$. The same limit on \dot{E} was also derived from first principles, showing that only very energetic pulsars can power PeV gamma-ray emission (de Oña Wilhelmi et al. 2022).

According to the ATNF database¹ (Manchester et al. 2005) there is no detected pulsar within 1° radius around LHAASO J2108+5157. This does not a priori exclude the PWN/TeV halo scenario, as the pulsar might remain undetected if its beam is not pointing towards us. The spectral analysis of Cao et al. (2021a) showed that a PWN scenario can also explain the observed UHE emission of LHAASO J2108+5157 and provided the lack of other observational data, especially missing VHE counterpart, the nature of the source remains unknown.

In this paper, we present results of a dedicated observation of the source region with the first Large-Sized Telescope (LST-1) and *XMM-Newton*², and also results of a dedicated analysis of *Fermi*-LAT data, providing strong constraints on LHAASO J2108+5157 gamma-ray and X-ray emission and the physical nature of the source. We also use all available data to carry out a detailed modeling of the multi-wavelength emission of the source, including a discussion of possible emission scenarios.

This paper is structured as follows: in Section 2 we describe detailed analysis of LST-1 and *Fermi*-LAT

¹<https://www.atnf.csiro.au/people/pulsar/psrcat/>

²Proposed as Target of Opportunity observation, PI: R. Walter.

data, followed by a dedicated analysis of the *XMM-Newton* data, and analysis of ^{12}CO (1-0) emission lines in the direction of the source collected in a composite survey of Dame et al. (2001). In Section 3 we present and discuss the results of multi-wavelength spectral modeling of the source. Finally, summary and conclusions can be found in Section 4.

2 Observations and data analysis

2.1 LST-1

LHAASO J2108+5157 was observed with LST-1 (López-Coto et al. 2021, LST Collaboration, in prep.) for 91 hours during 49 nights from June to September 2021. The data were taken in Wobble mode, which allows to evaluate the background from the same observations (Fomin et al. 1994), using four positions centered at R.A. = 317.15° , Dec = 51.95° , i.e. at coordinates between the LHAASO source and possible *Fermi*-LAT counterpart. The offset of each Wobble with respect to the center of the field of view (FoV) was 0.5° , instead of the standard 4° , to decrease the number of excess events leaking into the background regions in case the source turned to be extended. The observations presented were taken up to $> 55^\circ$ zenith angle, and with Moon below horizon. Quality cuts based on the stability of trigger rate, atmospheric transmission (using MAGIC LIDAR measurements (Fruck et al. 2022)) and rate of CR events were applied, resulting in 49.3 hours of good quality data (dead time corrected) used for the analysis.

The data calibration and shower reconstruction was carried out using the standard pipeline implemented in `1stchain v0.9` (López-Coto et al. 2022). To separate pixels containing Cherenkov light emitted by the atmospheric shower particles from background noise, the image cleaning taking into account the pixel-wise noise fluctuations was applied (LST Collaboration, in prep.). This method exploits background level information provided by dedicated interleaved pedestal events (containing only noise) acquired during observations at a rate of 100 Hz to reduce the effect of increased pixel noise due to e.g. stars in the FoV (LST Collaboration, in prep.). The cleaned shower images were parameterized with Hillas parameters (Hillas 1985). Then, Random Forests (RFs) trained on Monte Carlo (MC) simulated images of gamma and proton events were applied for the gamma/hadron separation (resulting in the so called Gammaness parameter estimation for each event)³, energy and arrival direction reconstruction of each event, using the Hillas parameters as inputs to the RF. As shower development for a primary particle/photon of given energy depends on the specific orientation of each shower relative to the local magnetic field, and the amount of Cherenkov light collected with the telescope depends on shower zenith angle, we trained the RFs on MC events simulated along a declination line, following the approximate path of the source in zenith and azimuth during the night (LST Collaboration, in prep.). While a constant low Night Sky Background (NSB) level was assumed in MC simulations, the real observations are performed in a wide range of NSB conditions. To reach the best possible performance in this particular analysis, we tuned the NSB levels in the training sample of MC simulated images on real data adopting the-so-called "noise padding" method (for further details see LST Collaboration, in prep.).

Global selection cuts on Gammaness⁴ and the squared angular distance between the reconstructed event direction and the source (θ^2) assuming point-like nature of the source were optimized on 36 high-quality runs of Crab Nebula observations taken in 2021, applying the same selection criteria as in the LHAASO J2108+5157 source analysis. Crab Nebula is the brightest persistent gamma-ray source in the sky, which makes it an ideal target for LST-1 calibration and validation of new data reconstruction methods (e.g. López-Coto et al. 2021; Emery et al. 2021; Juryšek et al. 2021). The Crab Nebula detection significance was evaluated on a grid of Gammaness $\in (0.5, 0.98)$ with a step of 0.02 and $\theta^2 \in (0.01, 0.1) \text{ deg}^2$ with a step of 0.002 deg^2 , resulting in the best global selection cuts of Gammaness > 0.84 and $\theta^2 < 0.04 \text{ deg}^2$ used in the spectral analysis. In order to reach the best possible performance for a potential source detection, we also optimized Gammaness cut on Crab detection significance in individual energy bins (5 bins per decade) keeping the θ^2 cut fixed.

θ^2 plot for three OFF regions reflected with respect to the center of the FoV after selection cuts optimized on Crab detection significance is shown in Figure 1. There is no significant source detection in either of the four energy bins, but at the highest energies (3 - 100 TeV), we see a hint of a source with 3.67σ detection

³Gammaness parameter indicates how likely it is that the event is created by a gamma ray, rather than a proton or other cosmic-ray particle.

⁴`1stchain` currently does not allow to apply energy dependent Gammaness cut optimized on a source detection significance to create data files in a format needed for `Gammapy` spectral analysis (DL3), and thus global cut was used in this case.

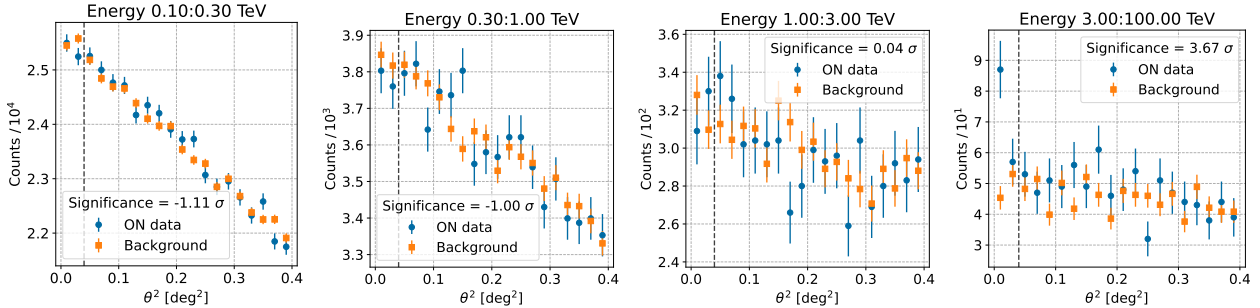


Figure 1: ON (blue) and OFF (orange) counts detected by LST-1 telescope after selection cuts in 49.3 hours of effective observation time in four blindly selected energy bins. Number of excess events in the first two θ^2 bins for the highest energies is 45 ± 13 with a Li&Ma detection significance of 3.67σ .

Data	Spectral model	N_0 [$\times 10^{-14} \text{cm}^{-2} \text{s}^{-1} \text{TeV}^{-1}$]	Γ	E_{cutoff} [TeV]	$-2 \log \mathcal{L}$
LST-1	PL	8.0 ± 5.4	1.62 ± 0.23	-	5.17
LST-1 + LHAASO	ECPL	7.6 ± 4.8	1.37 ± 0.22	50 ± 14	7.30

Table 1: Best fit parameters for the spectral analysis performed on the LST-1 data alone using PL model of the spectrum, and for the joint fit to LST-1 and LHAASO data using ECPL.

significance (Li & Ma 1983) and signal to noise ratio $S/N = 46\%$ under the point-like source assumption. This signal is not enough to claim a detection of the source in TeV energy range. However, if the excess above 3 TeV proves to be significant in future observations, then no excess seen at lower energies may suggest a hard spectral index of the potential VHE source.

2.1.1 Spectral analysis

We have performed a 1D spectral analysis using the `Gammapy` (Deil et al. 2017) package, adopting the source coordinates reported by Cao et al. (2021a). As LST-1 is in the commissioning phase and the analysis software and methods are still under intensive development, we performed only a preliminary 2D analysis using an acceptance model taken from real LST data, which was then used to correct for radial dependencies in the background models in `Gammapy`. The results of the 2D analysis can be found in Appendix A, but detailed analysis of the source morphology is left for future studies.

The 1D spectral analysis was performed in the energy range of 100 GeV to 100 TeV, using reflected region background method to estimate the number of background events in the signal region. We assumed the source spectrum to follow a single power law (PL) defined as $dN/dE = N_0(E/E_0)^{-\Gamma}$, with fixed reference energy $E_0 = 1 \text{ TeV}$. Having no morphological information and no sign of a potential source extension in the LST-1 data, the best-fit spectral parameters were found under the point-like source assumption. The resulting spectral parameters are listed in Table 1. Despite the large statistical uncertainties, the resulting photon indices suggest relatively hard spectrum in the TeV range. We estimated systematic uncertainty due to the energy resolution on the fitted photon index Γ to be $\sim 2\%$, and it is therefore negligible compared to the statistical uncertainty.

We also performed a joint likelihood fit of the LST-1 data and LHAASO flux-points to find out the spectrum of the source in the multi-GeV to multi-TeV range. Provided the hard TeV and soft multi-TeV spectrum, we considered as spectral shape a power law with an exponential cutoff (ECPL), defined as $dN/dE = N_0(E/E_0)^{-\Gamma} \exp(-E/E_{\text{cutoff}})$. The best fit parameters are listed in Table 1.

As a second step, we performed a maximum likelihood estimation of the source flux in 6 logarithmically spaced energy bins between 100 GeV and 100 TeV, using ECPL spectral parameters fitted in the previous step. We did not reach a significant source detection in TeV range, and thus we calculated 95% confidence level differential flux upper limits (ULs) in individual energy bins, shown in Figure 2. In the first energy bin (0.1–0.316 TeV) the telescope effective area drops below 10%, which we used as a safe threshold in the analysis, and thus the `Gammapy` flux point estimator only calculated fluxes in 5 energy bins. Table 2 summarizes LST-1 measured flux ULs and corresponding TS in each energy bin.

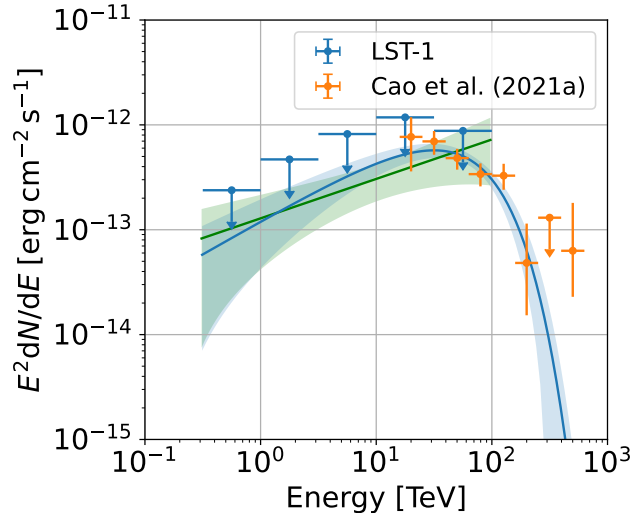


Figure 2: Spectral energy distribution of the LHAASO J2108+5157 source observed with LST-1. Green confidence band represents best fitting PL spectral model of LST-1 data and its statistical uncertainties. Joint likelihood fit of the LST-1 data and LHAASO flux-points with ECPL spectral model is represented by blue confidence band. 95% confidence level ULs on differential flux shown in all energy bins were estimated with the ECPL spectral model.

E min [TeV]	E max [TeV]	Flux ULs [$\times 10^{-14}$ cm $^{-2}$ s $^{-1}$]	TS
0.32	1.00	30.8	0.85
1.00	3.16	19.2	0.23
3.16	10.00	10.6	4.19
10.00	31.62	4.86	7.07
31.62	100.00	1.20	0.15

Table 2: LST-1 flux ULs (95% confidence level) assuming a point-like source with a ECPL spectral model.

Even though no significant point-like source was detected at energies above 300 GeV (2.2σ for PL spectral model), the LST-1 ULs provide strong constraints on the source emission, further discussed in Section 3. The resulting integral 95% UL on flux of the source is $F(E > 300 \text{ GeV}) < 5.0 \times 10^{-13} \text{ ph cm}^{-2} \text{ s}^{-1}$.

2.2 Fermi-LAT

We performed a dedicated binned analysis of this region with the publicly available *Fermi*-LAT science tools⁵. We followed the standard recommendations from the *Fermi*-LAT team to analyse data from 1 GeV up to 500 GeV, within 11° from the LHAASO source, in order to take into account the broad instrument Point Spread Function (PSF). We selected only data with `evclass=128` and `evtype=3`, with `zenith angle < 90°`. Data were covering the time interval from 4th August 2008 till 31st January 2022, and we filtered out bad time intervals using `(DATA_QUAL>0)&&(LAT_CONFIG==1)`. The data were reprocessed with the most recent P8R3_SOURCE_V3 IRF, and we used `gll_iem_v07`⁶ for the most updated Galactic diffuse emission model and `iso_P8R3_SOURCE_V3_v1` for the isotropic emission. We used a spatial binning of $0.1^\circ/\text{pixel}$ and 8 logarithmically uniform energy bins per decade. Differently from the LHAASO Collaboration that has used the 10-years 4FGL-DR2 catalogue (Ballet et al. 2020), in our analysis we have used the more recent 12-years 4FGL-DR3 catalogue (Fermi-LAT collaboration et al. 2022) to create the source model, which includes more sources. More specifically, the LHAASO team manually added two new γ -ray sources in their source model to describe

⁵<https://fermi.gsfc.nasa.gov/ssc/data/analysis/software/>

⁶<https://fermi.gsfc.nasa.gov/ssc/data/analysis/software/aux/4fgl/>
Galactic_Diffuse_Emission_Model_for_the_4FGL_Catalog_Analysis.pdf

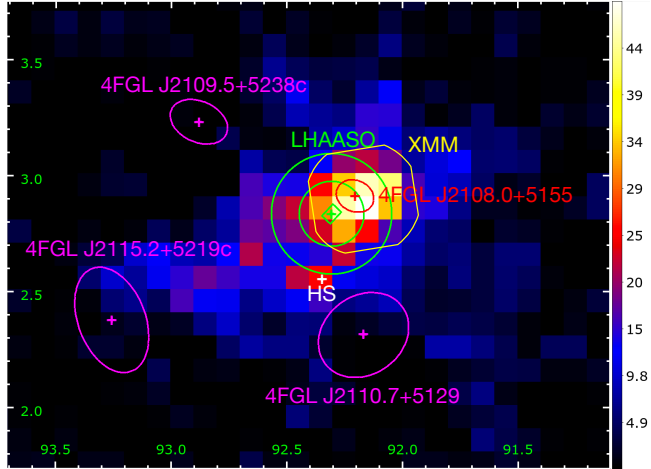


Figure 3: Fermi-LAT TS map in Galactic coordinate above 2 GeV, which shows the sources present in the 4FGL-DR3 catalogue with their 95% positional errors (magenta and red ellipses). The small green rectangle indicates the position of the LHAASO source with statistical uncertainty on R.A. and Dec derived from a two-dimensional Gaussian model, while the smaller green circle represents 95% position uncertainty of 0.14° reported by Cao et al. (2021a). The larger green circle indicates the 95% UL on the source extension (0.26°). The white cross highlights the position of a new potential hard source, whereas the yellow contour indicates the FoV of the previously discussed XMM observation.

the region of interest (ROI), found with the "find source" tool of `fermipy` (Wood et al. 2017). One of the two sources visible in their plot (see bottom left square in the left of Figure 6 of Cao et al. (2021a)) is now confirmed in the new DR3 catalogue as an interstellar gas clump, but with slightly shifted coordinates (4FGL J2115.2+5219c). The other source does not appear in the new *Fermi*-LAT catalogue, and it is also not detected in our analysis. As recommended, we included sources in our xml model up to 5° beyond our ROI, keeping their parameters frozen in the likelihood fit.

Any source in the catalogue with non-zero `flags` parameter indicates that it is affected by systematic errors. Sources with these indicators should be used with great care. They correspond to significant excesses of photons, but such excesses can result from residual extended emission or confused source pile-up. In the 4FGL-DR3 catalogue, three sources within less than 1.5° from LHAASO J2108+5157 are flagged with "c", which stands for "interstellar gas clump". More than 50% of the neighbouring sources within less than 4° from LHAASO J2108+5157 present at least one non-zero flag (for more details see Fermi-LAT collaboration et al. 2022), which make the low-energy *Fermi*-LAT analysis non-trivial.

Looking at all sources present in the 4FGL-DR3 catalogue and their 95% positional error, there are no counterparts overlapping with the uncertainty position provided by LHAASO (see Figure 3). The closest source is 4FGL J2108.0+5155 which lies 0.13° away. Above 1 GeV, the source spectrum is well fitted by a LogParabola with normalization of $(9.8 \pm 0.9) \times 10^{-13}$ ph/cm²/s/MeV, $\alpha = 2.5 \pm 0.2$ and $\beta = 0.37 \pm 0.18$, assuming the same E_b value equal to the catalogue (i.e. $E_b = 1580.67$ MeV). The other three 4FGL sources visible in Figure 3 are fainter and present a softer log-parabolic spectrum with a turnover at lower energies, with the only exception of J2109.5+5238c, whose spectrum is a PL with photon index of 2.6, which locally overtakes the flux of 4FGL J2108.0+5155 above few tens of GeV.

The spectrum of the closest source to LHAASO J2108+5157, i.e. 4FGL J2108.0+5155 presents a steep decrease above few GeVs, not compatible with the UHE LHAASO points. Therefore, its physical relation to the UHE source is challenging (see Discussion in the next sections). Re-running the analysis, extending the low-energy threshold to 500 MeV and to 300 MeV, properly increasing and adapting the selected ROI, the fitted spectra that we obtain present some scatters at low energy, due to the large instrument PSF. It depends on how much freedom we allow in the fit to the neighbour sources and to the Galactic diffuse emission, but in all cases the trend converges toward a unique and consistent behaviour above few GeVs.

In order to verify the goodness of the used source model at high energies, we performed a $15^\circ \times 15^\circ$ TS map, centered on the LHAASO source, removing the source 4FGL J2108.0+5155 from the model. We computed the TS map above different threshold energies, from 1 GeV to 10 GeV, and we used a PL spectrum for the putative

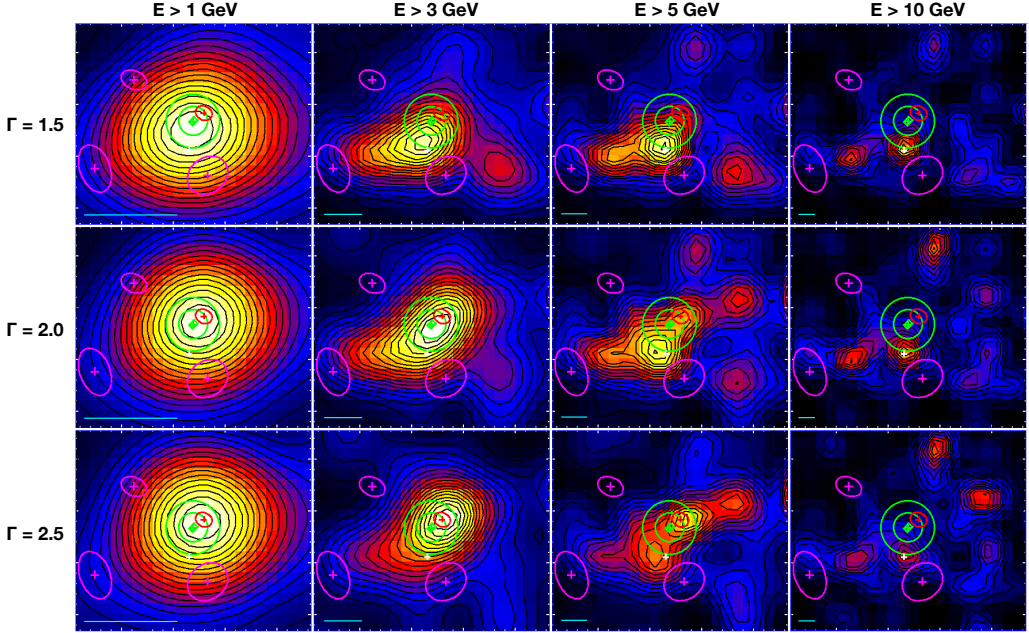


Figure 4: *Fermi*-LAT TS maps computed assuming various photon indexes for the putative source, and above different threshold energies. Each TS map is smoothed with a Gaussian whose sigma is equal to 68% of the *Fermi*-LAT PSF containment radius measured at each corresponding threshold energy. This size is reported with a cyan segment in the bottom left corner of each plot. Black contours are overplotted with a linear scale to better localize the position of the TS peaks. Green, red, magenta and white elements are the same used and described in Figure 3. The white small ticks on both axes are in unit of 0.1° . Each subplot have been renormalised to its own maximum value to make their colorscale and isocontours comparable.

source, assuming different gamma indices (from -1.5 to -3). Some of these TS maps are reported in Figure 4. Each TS map has been smoothed with a Gaussian with a standard deviation equal to 68% of the *Fermi*-LAT containment angles at each different threshold energy. From this analysis we can clearly see that, assuming a very soft photon index, above 1 GeV the peak of the TS map coincides with the position of 4FGL J2108.0+5155, whereas using a harder photon index the peak moves toward South-East (in Galactic coordinates). This trend becomes even more evident when we move towards higher energies. Already above 2 GeV the excess of the TS maps assumes an elongated shape toward South-East, and cannot be considered as point-like anymore, neither can it be reproduced by an extended symmetric Gaussian. These TS maps (Figure 4) confirm the very soft spectral behaviour of 4FGL J2108.0+5155, whose flux steeply drops above few GeVs, and suggest the presence of two different sources with clearly distinct spectra, located at two different positions, separated by $\sim 0.4^\circ$. One of these sources is 4FGL J2108.0+5155, already included in the 4FGL-DR3 catalogue, whereas the other is a new hard source (hereafter HS), approximately located at $l = 92.35^\circ$ and $b = 2.56^\circ$, not included in the catalogue. Such sources get confused at low energy due to the relatively large PSF of the *Fermi*-LAT instrument, and it is not trivial to spatially disentangle them. On the contrary, they are clearly distinguishable above few GeVs, where the PSF becomes smaller than the two source separation⁷. The existence of two distinct peaks is evident also in the non-smoothed TS maps. Assuming a flat spectrum, the excess at the position of HS dominates over the one of 4FGL J2108.0+5155 above ~ 4 GeV. If instead we assume a harder spectrum, such transition occurs at even lower energies. It is important to mention that the new HS source does not spatially correlate with the local structure of the diffuse Galactic emission model.

Adding the new HS source in the original source model and re-running the likelihood fit analysis provides slightly different results for the spectral shape of 4FGL J2108.0+5155, which is now fitted with a LogParabola with normalization of $(9.9 \pm 0.9) \times 10^{-13}$ ph/cm²/s/MeV, $\alpha = 2.7 \pm 0.2$ and $\beta = 0.32 \pm 0.16$, assuming the same fixed E_b value. The new HS source is detected with a significance of $\sim 4\sigma$, and its spectrum could be fitted

⁷As a matter of reference, 0.4° corresponds to more than 68% containment angle above 3 GeV for the *Fermi*-LAT instrument. At higher energies the PSF decreases, reaching 0.2° and better above 10 GeV. For detailed *Fermi*-LAT PSF dependence on energy see: https://www.slac.stanford.edu/exp/glast/groups/canda/lat_Performance.htm

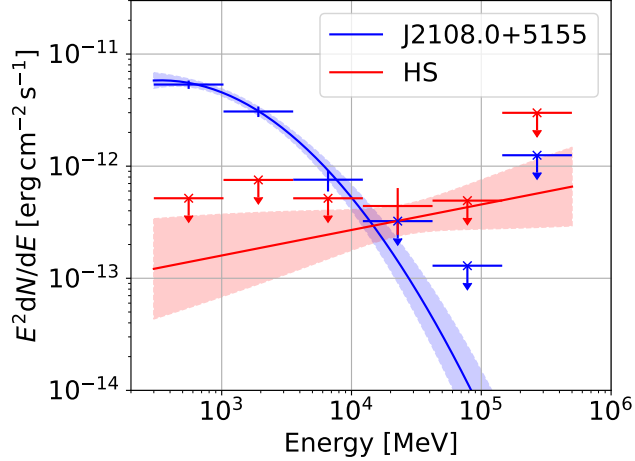


Figure 5: *Fermi*-LAT SED for J2108.0+5155 (blue) and HS (red) analyzed with the energy threshold of 300 MeV (see the text for details). Fluxes in energy bins with $TS > 10$ are drawn as flux points, for lower TS 95% confidence level ULs are shown.

with a PL with normalization $(1.5 \pm 0.9) \times 10^{13}$ ph/cm²/s/MeV and photon index $\Gamma = 1.9 \pm 0.2$, using an energy scale $E_0 = 1$ GeV. If we fix the photon index, the normalization accuracy of HS improves to $(1.5 \pm 0.5) \times 10^{-13}$ ph/cm²/s/MeV. Due to the HS small flux at low energies, its inclusion in the model does not affect much the spectral results of the neighbour sources, in particular at low energies. Using a different model to represent the HS source, like e.g. a LogParabola or ECPL does not improve the likelihood fitting, so the simple PL which presents fewer degrees of freedom is preferred. The angular separation of this HS from the LHAASO J2108+5157 source is 0.27° , which is larger than the 95% upper limit of the extension provided in Cao et al. (2021a), and therefore can hardly be its counterpart.

The SED points of J2108.0+5155 and HS shown in Figure 5, have been computed running a separate independent likelihood analysis in each smaller energy band, assuming the same source model obtained from the full energy band fit, but replacing the source of interest with a simple PL spectrum. Its normalization was let free to vary in the fit, whereas its photon index was fixed to the local slope (α) of the LogParabola, in the case of J2108.0+5155, and to the previous obtained photon index Γ , in the case of the HS source. The error bar represents 1σ statistical error. The confidence band, represents the 1σ error, obtained from the covariance matrix of the fit.

The discrepancy between our flux and the one provided by Cao et al. (2021a) can arise from the several differences present between the two analyses, which we have highlighted in this article. In particular, we used a more recent IRF, a more recent source catalogue, and a more recent isotropic diffuse emission component. Furthermore, Cao et al. (2021a) provided the integral flux value assuming a symmetric Gaussian extended source with radius of 0.48° , that our TS map results reveal not to be a correct assumption (see Figure 4).

2.3 XMM-Newton

The field surrounding LHAASO J2108+5157 was observed by *XMM-Newton* on June 11, 2021 for a total of 13.6 ks. The observation was centered on R.A.(J2000)= 317.0170° , Dec(J2000)= $+51.9275^\circ$. We reduced the data from the European Photon Imaging Camera (EPIC)⁸ of *XMM-Newton* using XMMSAS v19.1 and the X-COP data analysis pipeline (Eckert et al. 2017; Ghirardini et al. 2019). After screening the data and creating calibrated event files using the standard chains, we used the XMMSAS tasks `pn-filter` and `mos-filter` to filter out time periods affected by strong soft proton flares. After excising the flaring time periods, the clean exposure time is 4.7 ks (MOS1), 4.9 ks (MOS2), and 3.0 ks (pn). From the clean event files, we extracted images in the soft (0.5-2 keV) and hard (2-7 keV) bands, and used the `eexpmap` task to create effective exposure maps accounting for vignetting, bad pixels, and chip gaps. To estimate the non X-ray CR induced background (NXB), we make use of the unexposed corners of the detectors to rescale the filter-wheel-closed event files available in the calibration database. We then reproject the filter-wheel-closed data to match the attitude file

⁸The EPIC is made of three co-aligned detectors: MOS1, MOS2 and pn.

of our observation and extract model particle background images from the rescaled filter-wheel-closed event files. Finally, we summed up the images of the three EPIC instruments as well as the NXB maps. We also created a total EPIC exposure map by summing up the exposure maps of the three instruments, weighted by their respective effective area.

We ran the XMMSAS task `ewavelet` to detect X-ray sources in the field. The resulting catalogue contains 11 sources in the soft band and 2 in the hard band. The brightest source in the field is associated with the eclipsing binary star V* V1061 Cyg (RX J2107.3+5202). We extracted the spectrum of the source and fitted it in XSPEC. We found that the eclipsing binary exhibits a very soft spectrum, which appears better represented by a thermal model with $kT \sim 0.8$ keV than with a PL. The total model flux of the source is 3.7×10^{-13} erg cm $^{-2}$ s $^{-1}$ (0.5-2 keV) and 2.0×10^{-14} erg cm $^{-2}$ s $^{-1}$ (2-7 keV). Assuming a thermal nature of the spectrum, this is an unlikely counterpart for the LHAASO source. The other sources in the field are substantially fainter than the fluxes reported here.

In case the source is associated with leptonic emission from a supernova remnant or PWN, we would expect the corresponding X-ray source to be extended. We therefore attempted to place upper limits on the possible X-ray flux of an extended source with varying radius and centered on the LHAASO source position. To this end, we used the public code `pyproffit` (Eckert et al. 2020) to extract the brightness profile of unresolved emission across the field. The NXB-subtracted, vignetting corrected profiles are consistent with a flat brightness distribution, which is compatible with the expected sky background emission made of a combination of the local hot bubble, the Galactic halo, and the cosmic X-ray background. In case the source is smaller than the *XMM-Newton* FoV (30' in diameter), we can use the measured count rates in the outer regions of the field to estimate the local sky background emission and set the maximum allowed number of source counts on top of the background. For aperture photometry performed in the Poisson regime, the signal-to-noise ratio is given by

$$S/N = \frac{N_{\text{src}}}{\sqrt{N_{\text{src}} + N_{\text{bkg}}}} \quad (1)$$

with N_{src} the number of (background-subtracted) source counts and N_{bkg} the total number of background counts (sky background + NXB). A 2σ upper limit can thus be set by computing the number of source counts for which $S/N=2$, i.e.

$$N_{2\sigma} = 2 + 2\sqrt{1 + N_{\text{bkg}}} \quad (2)$$

For a uniform, circular source the corresponding upper limit depends on the assumed source radius since the background expectation is proportional to the area. We computed such upper limits for three possible apertures: a radius of 0.5 arcmin (point-like source) and extended sources with radii of 3 and 6 arcmin, respectively. The estimated 2σ upper limits on the allowed number of counts and count rates are given in Table 3.

To convert the upper limits on the count rates into fluxes, a model spectrum needs to be assumed, and especially, it needs to be understood whether the source is affected by Galactic extinction or not. In case the source is located at the opposite side of the Galaxy, the measured X-ray fluxes will be attenuated by the Galactic N_H , which is substantial along the Galactic plane. The Galactic HI column density at the position of the LHAASO source is 1.05×10^{22} cm $^{-2}$ (HI4PI Collaboration et al. 2016), which implies that the majority of low-energy photons will be absorbed along the way, such that the actual emitted flux can be substantially higher. Conversely, in case the source is local the source spectrum will be essentially unabsorbed. Here we provide upper limits for the two extreme cases of a completely absorbed and a completely unabsorbed source to bracket all possible scenarios. We simulated *XMM-Newton* spectra assuming that the source spectrum is a PL with a photon index of 2.0 and computed the conversion between count rate and flux in the two energy bands and for the absorbed and unabsorbed scenarios alike. The conversion factors were then used to determine the corresponding flux upper limits. In Table 3 we provide a list of upper limits for a wide range of scenarios. The allowed values are in the range $10^{-15} - 10^{-13}$ erg cm $^{-2}$ s $^{-1}$ depending on the assumed source size and spectrum.

2.4 Molecular clouds

LHAASO J2108+5157 is located in a direction of relatively dense molecular clouds. Cao et al. (2021a) searched the database of molecular clouds in Galactic plane (Miville-Deschénes et al. 2017) and found its position close

Radius arcmin	$N_{\text{src},0.5-2}$ cts	$CR_{0.5-2}$ cts s ⁻¹	$F_{0.5-2,\text{abs}}$ erg cm ⁻² s ⁻¹	$F_{0.5-2,\text{unabs}}$ erg cm ⁻² s ⁻¹	$N_{\text{src},2-7}$ cts	CR_{2-7} cts s ⁻¹	$F_{2-7,\text{abs}}$ erg cm ⁻² s ⁻¹	$F_{2-7,\text{unabs}}$ erg cm ⁻² s ⁻¹
0.5	10.214	5.940e-4	1.69e-14	2.36e-15	10.014	6.391e-4	1.28e-14	1.04e-14
3	47.415	3.070e-3	8.76e-14	1.22e-14	47.892	3.380e-3	6.77e-14	5.51e-14
6	88.527	6.464e-3	1.84e-13	2.57e-14	90.055	7.221e-3	1.45e-13	1.18e-13

Table 3: *XMM-Newton* 2σ upper limits on number of counts, count rate (CR), and the X-ray flux of the LHAASO source for varying source apertures, energy bands and source emission models. The fluxes are estimated assuming that the source spectrum can be described by a PL with a photon index of 2.0, either on the other side of the Galaxy (i.e. absorbed by the local Galactic column density) or local (unabsorbed). In the absorbed case, the corresponding flux is the equivalent unabsorbed source flux.

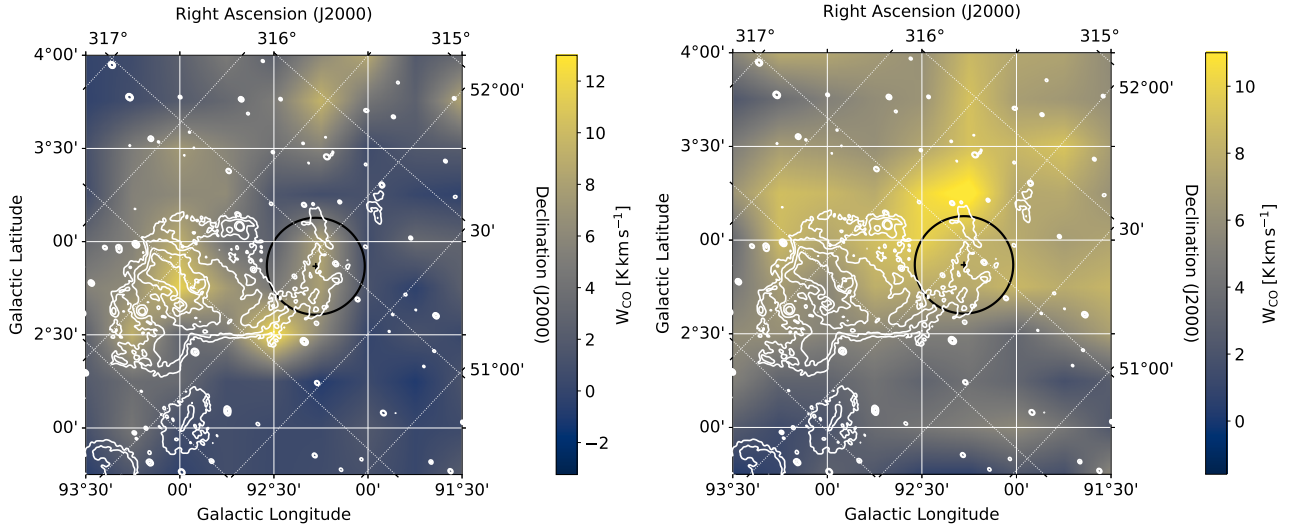


Figure 6: Velocity integrated ^{12}CO intensity (W_{CO}) of two molecular clouds spatially coincident with the direction of LHAASO J2108+5157. *Left:* Integrated velocity of the first Gaussian component peaking at $v_1 \approx -11.8 \text{ km s}^{-1}$, with corresponding distance of $d_1 \approx 3.1 \text{ kpc}$. *Right:* Integral of the second Gaussian component at $v_2 \approx -2.7 \text{ km s}^{-1}$ and $d_1 \approx 2.0 \text{ kpc}$. The white contour represents 1420 MHz continuum emission from the Canadian Galactic Plane Survey (CGPS) (Taylor et al. 2003). Position of LHAASO J2108+5157 is marked with a black cross, and 95% UL on its extension (0.26°) is indicated with a black circle (Cao et al. 2021a). Bilinear interpolation is used to smooth out contribution of individual pixels.

to the direction of two molecular clouds [MML2017]2870 and [MML2017]4607 with distances 1.43 kpc and 3.28 kpc, and masses $3.5 \times 10^4 \text{ M}_\odot$ and $8.5 \times 10^3 \text{ M}_\odot$, respectively.

To estimate the total gas density in the direction of LHAASO J2108+5157, we considered contribution of H_2 molecular density and density of neutral hydrogen HI. We used $^{12}\text{CO}(1-0)$ line emission observations collected in a composite survey of Dame et al. (2001) to estimate density and distance of the molecular clouds. Note that provided Galactic longitude of the source $l > 90^\circ$, kinematic distance of each molecular cloud has only a single solution (see e.g. Roman-Duval et al. 2009). In order to get a mean radial velocity spectrum of brightness temperature $T_B(v)$ in the direction of the source, we averaged over the 95% ULs on extension of the UHE source 0.26° reported by Cao et al. (2021a). Consistently with Cao et al. (2021a) we identified three peaks in the $T_{B(\text{H}_2,v)}$ spectrum, which can be well described by three Gaussians at $v_1 \approx -11.8 \text{ km s}^{-1}$, $v_2 \approx -2.7 \text{ km s}^{-1}$ and $v_3 \approx 8.4 \text{ km s}^{-1}$. Two of those correspond to the centroid velocities of the molecular clouds -1.1 km s^{-1} and -13.7 km s^{-1} identified by (Miville-Deschénes et al. 2017), but origin of the last peak remains unknown, and we further consider only the clouds with negative radial velocities.

For determination of kinematic distances d to the molecular clouds, we adopted power law rotation curve (Russeil et al. 2017) with galactocentric radius $R_0 = 8.34 \text{ kpc}$ and orbital velocity of the Sun $V_0 = 240 \text{ km s}^{-1}$, leading to $d_1 \approx 3.1 \text{ kpc}$ and $d_2 \approx 2.0 \text{ kpc}$. The angular radius of the UHE emission can be then converted to physical radius of the source $r_1 = 7.1 \text{ pc}$ and $r_2 = 4.5 \text{ pc}$, depending on its distance, if spatially coincident with

the molecular clouds.

In order to get average densities of the molecular clouds in the source region, we integrated the individual Gaussian contributions W_{CO} over velocity ranges $v_1 \in (-23, -1) \text{ km s}^{-1}$ and $v_2 \in (-9, 4) \text{ km s}^{-1}$, given by 3σ ranges of the two Gaussian contributions. W_{CO} can be then converted into the column density as $N(\text{H}_2) = X_{\text{CO}} W_{\text{CO}} / N_{\text{px}}$, where $X_{\text{CO}} = 2 \times 10^{20} \text{ cm}^{-2} \text{ s K}^{-1} \text{ km}^{-1}$ (Bolatto et al. 2013), and N_{px} is number of pixels on the sky within the source extension. Assuming a spherically symmetrical source emission region, we estimate the number density of molecular hydrogen $n_1(\text{H}_2) = N_1(\text{H}_2) / 2r_1 = 51 \text{ cm}^{-3}$ and $n_2(\text{H}_2) = 170 \text{ cm}^{-3}$, for the distant and the close molecular cloud, respectively. Skymap of velocity integrated ^{12}CO intensity is shown in Figure 6 for both molecular clouds.

To estimate density of neutral hydrogen HI, we used brightness temperature velocity spectrum $T_{\text{B(HI,v)}}$ in the direction of the source averaged over its angular extension from the HI4 π survey (HI4PI Collaboration et al. 2016). Column density of HI can be estimated under the optically thin limit assumption as $N(\text{HI}) = 1.823 \int T_{\text{B(HI,v)}} \text{ dv cm}^{-2}$ (Dickey & Lockman 1990). Assuming the same distance for both gas phases, we integrated over the same velocity ranges as for the H_2 molecular clouds. Following the same geometrical assumptions as for H_2 , we estimate number density of neutral hydrogen as $n_1(\text{HI}) = 64 \text{ cm}^{-3}$ and $n_2(\text{HI}) = 70 \text{ cm}^{-3}$. The total number density of gas in the source region can be hence estimated for both clouds as $n_1 = n_1(\text{HI}) + n_1(\text{H}_2) = 115 \text{ cm}^{-3}$ and $n_2 = 240 \text{ cm}^{-3}$.

3 Spectral modeling and discussion

3.1 Leptonic scenario of emission

Provided that most of the VHE sources in our Galaxy have been identified as Pulsar Wind Nebulae (PWNe) (H. E. S. S. Collaboration et al. 2018c), we first examine this scenario of emission. Here we provide quantitative estimates and limits on leptonic scenario of emission derived from the data, and compare them with the physical properties of known PWNe/TeV halos.

We used the `naima`⁹ package (Zabalza 2015) to derive a parent electron distribution reproducing IC dominated (Khangulyan et al. 2014) VHE to UHE emission of LHAASO J2108+5157. For the sake of simplicity, we assume a single electron spectrum in a form of ECPL $f(E) \sim E^{-\alpha} \exp(-E/E_c)$. As the source was not detected in the X-ray range, we only considered IC emission using the LST-1 and LHAASO flux points (Cao et al. 2021a). The target photon field for IC is expected to consist of CMB and Far Infrared Radiation of the dust (FIR), with temperatures of 2.83 K and 20 K, and energy densities of 0.26 eV cm^{-3} and 0.3 eV cm^{-3} , respectively, which are typical values at Galacto-centric radius of the Sun (Hinton & Hofmann 2009; Popescu et al. 2017).

The electron distribution that best describes the observations is shown in Figure 7. It has a cutoff at $E_c = 100_{-30}^{+70} \text{ TeV}$ and spectral index $\alpha = 1.5 \pm 0.4$. All parameters of the model are summarized in Table 4. If magnetic field is present, the same population of electrons must emit synchrotron radiation (Aharonian et al. 2010), which together with the *XMM-Newton* upper limits on the X-ray emission allow us to put constraint on magnetic field strength in the PWN. Figure 7 shows 95% *XMM-Newton* upper limits on the absorbed emission in a circular region with $r = 6'$, which is a reasonable upper limit on the angular size of a Galactic PWN emitting X-rays at a distance $d \leq 10 \text{ kpc}$ (Bamba et al. 2010). The comparison with the 95% CL of synchrotron emission constrains the magnetic field to $B \lesssim 1.2 \mu\text{G}$, which is lower than a typical value of Galactic magnetic field $B_{\text{G}} \approx 3 \mu\text{G}$. Note that for unabsorbed X-ray upper limits, relevant if the source is relatively close, the constraints on the magnetic field would be even stronger $B \lesssim 0.5 \mu\text{G}$. Provided the Galactic latitude $b \approx 3^\circ$, the source is close to the Galactic plane if it is not too distant from the Sun, and one should not expect a background magnetic field strength significantly below the typical level, and thus the absorbed case seems to be favored. We cannot, however, exclude the possibility of larger extension of the undetected PWN, which would lead to more relaxed constraints on its magnetic field.

In the PWN scenario, the lack of detectable X-ray emission can be explained if the pulsar is relatively old. The electron population which has been injected into the nebula during its lifetime is subject to radiative cooling, which leads to reduction of the HE electrons responsible for the X-ray emission. In addition, spin-down power of pulsar decreases in time, and hence the supply of fresh HE electrons is reduced over time (Pacini

⁹<https://naima.readthedocs.io/>

Parameter	Best fit value	Frozen
E_0 [TeV]	1	True
$E_{e,\min}$ [GeV]	0.1	True
$E_{e,\max}$ [TeV]	1000	True
N_0 [$\times 10^{43}$ TeV $^{-1}$]	$1.7^{+4}_{-1.4}$	False
E_c [TeV]	100^{+70}_{-30}	False
α	1.5 ± 0.4	False

Table 4: Best fit parameters of ECPL electron distribution in the form $dN/dE = N_0(E/E_0)^{-\alpha} \exp(-(E/E_c))$, where E_0 is the energy scale, α the spectral index, and E_c the cutoff energy. Normalization of the spectrum N_0 is calculated for the source distance of 1 kpc. VHE-UHE emission of LHAASO J2108+5157 is assumed to be dominated by emission due to IC scattering of electrons on CMB ($T = 2.83$ K, $u = 0.26$ eVcm $^{-3}$) and FIR ($T = 20$ K, $u = 0.3$ eVcm $^{-3}$) seed photon fields.

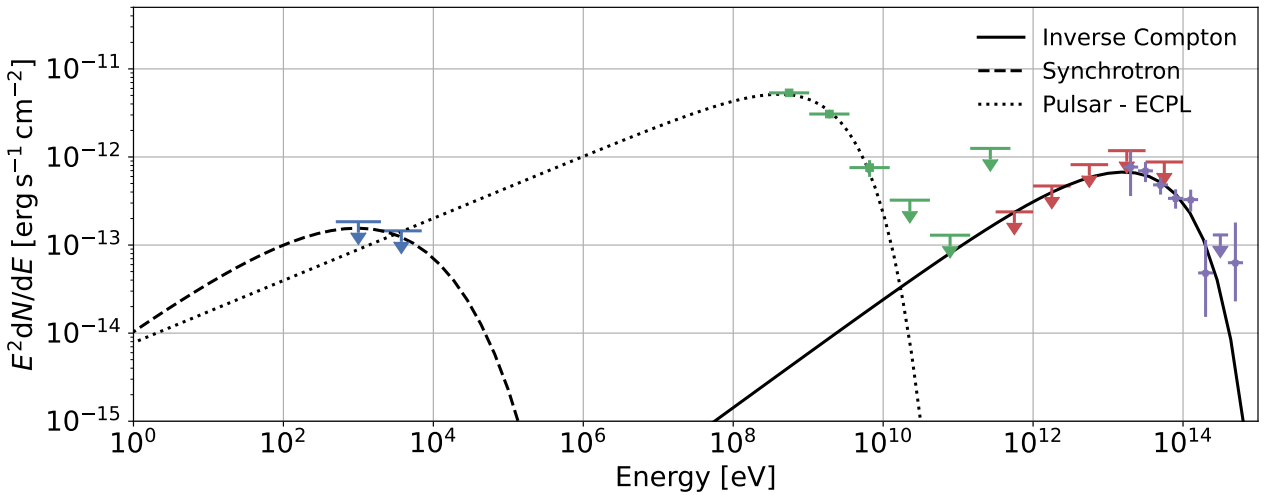


Figure 7: Multi-wavelength SED of LHAASO J2108+5157 showing leptonic scenario of emission. Observations with different instruments are represented by datapoints of different colours - *XMM-Newton* $r = 6'$ (blue), *Fermi*-LAT (green), LST-1 (red), LHAASO-KM2A (purple). Black line represents the best fitting IC dominated emission of LST-1 and LHAASO data, dashed line represents the corresponding synchrotron radiation of the same population of electrons for $B = 1.2 \mu\text{G}$. Dotted line represents a phenomenological model of tentative pulsar - the best fit of power law with sub-exponential cutoff on the *Fermi*-LAT data.

& Salvati 1973). Evolution of the pulsar spin-down power, together with expansion of PWN leads also to a decrease of the magnetic field strength, which further suppresses synchrotron emission from the electrons (e.g. Zhang et al. 2008; Mayer et al. 2012). For these reasons old PWNe become fainter in X-rays and may become undetectable in this band, even though VHE gamma-ray emission of such sources can still be detected due to the IC radiation of accumulated low energy electrons (de Jager & Harding 1992; Mattana et al. 2009).

It has been shown by Mattana et al. (2009) that due to the scaling of the X-ray luminosity with spin-down power of the pulsar, the ratio of gamma-ray (L_γ) to X-ray luminosity (L_X) is correlated to the pulsar characteristic age τ_c and anti-correlated to spin-down power \dot{E} . The observed gamma-ray luminosity of LHAASO J2108+5157 and the upper limits on the synchrotron emission give $L_{\gamma, (1-30\text{TeV})}/L_{X, (2-10\text{keV})} \geq 10$, and thus provide a lower limit on $\tau_c \geq 10^4$ yr. A more recent study of Kargaltsev et al. (2013) on X-ray and TeV γ -ray emission of Galactic PWNe provides similar constraints on the age of the nebula and upper limit on $\dot{E} \leq 10^{37}$ erg s $^{-1}$, which is within the range of values typical for pulsars identified with PWNe observed by the H.E.S.S experiment (H. E. S. S. Collaboration et al. 2018a).

It is challenging to explain the weak magnetic field $B \lesssim 1.2 \mu\text{G}$ needed to suppress the synchrotron emission of LHAASO J2108+5157 in the PWN scenario, where a typical level of B ranges between 1 – 100 μG (Martin et al. 2014; Zhu et al. 2018). We note, however, that a relatively weak magnetic field is needed to explain a leptonic UHE emission, which is only possible in the radiation dominated environments (Vannoni et al. 2009; Breuhaus et al. 2021, 2022). MILAGRO (Abdo et al. 2009) and HAWC (Abeysekara et al. 2017) detected an extended 2° TeV emission surrounding Geminga pulsar, leading to a recent establishment of a new class of TeV-halo sources (Linden et al. 2017). We note that TeV PWNe showing a larger extension than that predicted in the PWN theory were known even before establishment of TeV-halos as a new class of sources (H. E. S. S. Collaboration et al. 2018a; Sudoh et al. 2019). Provided the TeV-halo extension, the expected strength of magnetic field in such sources is significantly lower than in compact PWNe and the SED is therefore dominated by TeV emission. Similarly to the case of LHAASO J2108+5157, Liu et al. (2019) obtained an upper limit on the magnetic field in the Geminga halo $B < 1 \mu\text{G}$, based on X-ray upper limits on the synchrotron emission. The TeV nebula surrounding Geminga pulsar has a large angular extension, but it is also relatively close ($d = 250$ pc (Faherty et al. 2007)). In the Geminga-like scenario, the lower limit on the distance of LHAASO J2108+5157 is approximately 2 kpc in order not to violate the source extension UL of 0.26° provided by Cao et al. (2021a).

IC dominated radiation of a single electron population cannot explain soft GeV emission of 4FGL J2108.0+5155, which is spatially coincident with LHAASO J2108+5157. There are 117 gamma-ray pulsars identified in the *Fermi*-LAT data, showing similar spectral properties as 4FGL J2108.0+5155 (Abdo et al. 2013). We therefore raise a hypothesis, that the GeV emission is a signature of a gamma-ray pulsar. Saz Parkinson et al. (2016) applied machine learning methods to classify sources in the Third *Fermi*-LAT catalog in two major classes: AGNs and pulsars. 3FGL J2108.1+5202, which is the Third *Fermi*-LAT general catalog (Acero et al. 2015) counterpart of 4FGL J2108.0+5155, was classified consistently with Logistic Regression (LR) and Random Forest (RF) classifiers as a pulsar, which gives a hint in favour of our hypothesis. We note, however, that resulting LR and RF probabilities are relatively low, only about 30 %, and thus we cannot exclude the possibility of miss-classification of the source, and extra-galactic origin of the HE emission cannot be excluded (for further details see Saz Parkinson et al. 2016).

Gamma-ray pulsars are characterized by a soft spectra, with the flux steeply falling above few GeV (e.g. MAGIC Collaboration et al. 2020). In the *Fermi*-LAT energy band, the typical differential spectrum can be described with a power law with sub-exponential cutoff $dN/dE = N_0(E/E_0)^{-\Gamma} \exp(-(E/E_{\text{cutoff}})^b)$, where E_0 is the energy scale, Γ the photon index, E_{cutoff} the cutoff energy, and b the cut-off strength (Leung et al. 2014; MAGIC Collaboration et al. 2020). In order to reduce degeneracy of the model parameters, considering that there are only three significant *Fermi*-LAT flux points, we fixed $b = 0.7$, which is the cut-off strength of power law with sub-exponential cutoff model of the Geminga pulsar SED in the GeV band (MAGIC Collaboration et al. 2020). The best fit of the *Fermi*-LAT data consistent with *XMM-Newton* ULs shown in Figure 7 has $\Gamma = 1.5^{+0.1}_{-0.2}$ and $E_{\text{cutoff}} = 0.9 \pm 0.2$ GeV. Despite the large uncertainty, the photon index is consistent with that of gamma-ray pulsars with spin-down power $\dot{E} = 10^{34} - 10^{37}$ erg s $^{-1}$ (Abdo et al. 2013). The gamma-ray luminosity of 4FGL J2108.0+5155 between 1-100 GeV is $L_{1-100\text{GeV}} = 2 \times 10^{33} (d/1\text{kpc})^2$ erg s $^{-1}$. One should note that assuming Galactic origin of the source, the Galactic longitude of the source $l = 92.2^\circ$, imply an UL on the source distance of $d \lesssim 8$ kpc, due to the geometrical reasons imposed by the position of the Sun in the Galaxy. It leads to an UL on the source luminosity of $L_{1-100\text{GeV}} \lesssim 1.3 \times 10^{35}$ erg s $^{-1}$, which is consistent with

the population of gamma-ray pulsars for any possible distance to the source.

The allowed spin-down power range of the tentative pulsar also implies limits on the luminosity in the TeV band $L_{1-10\text{TeV}} \approx 10^{31} - 10^{35} \text{ erg s}^{-1}$ of the nebula powered by the pulsar, when compared with the sample of known TeV PWNe (see Figure 7 in H. E. S. S. Collaboration et al. 2018a). TeV luminosity of LHAASO J2108+5157 is $L_{1-10\text{TeV}} \approx 6 \times 10^{32} (d/1\text{kpc})^2 \text{ erg s}^{-1}$, which makes the pulsar scenario valid for any possible distance of the source within the Galaxy. In the Geminga-like scenario, assuming the source extension of the order of 10 pc, the minimum possible distance of 2 kpc implies TeV PWN luminosity $L_{1-10\text{TeV}} > 2 \times 10^{33} \text{ erg s}^{-1}$ and thus the pulsar spin-down power $\dot{E} > 10^{35} \text{ erg s}^{-1}$, consistently with the expectations derived from the SED of the *Fermi*-LAT counterpart.

The total energy in electrons dominating the TeV emission is $E(> 1\text{ GeV}) \approx 1 \times 10^{45} (d/1\text{kpc})^2 \text{ erg}$, which can be compared with the total energy released by the pulsar during relativistic electron IC cooling time, given by

$$t_{\text{cool,yr}} \approx 3.1 \times 10^5 (1 + 40E_{\text{e,TeV}}(kT)_{\text{eV}})^{1.5} u_{\text{rad,eVcm}^{-3}}^{-1} E_{\text{e,TeV}}^{-1}, \quad (3)$$

where E_{e} is electron energy, and u_{rad} and T are energy density and temperature of the radiation field, respectively (Moderski et al. 2005; Hinton & Hofmann 2009). For the cutoff energy electrons $E_{\text{c}} = 100\text{TeV}$ and CMB radiation field, we get $t_{\text{cool}} \approx 30\text{ kyr}$. The total energy released by the pulsar would be in the range of $E \approx 10^{47} - 10^{49} \text{ erg}$, for the spin-down power in the range of $\dot{E} \approx 10^{35} - 10^{37} \text{ erg s}^{-1}$. Provided that the distance to the source would be $d \leq 10\text{kpc}$, only a small fraction of the total energy released by the pulsar during its lifetime needs to be invested in acceleration of the high energy electrons.

The physical size of the TeV halo can be estimated assuming diffusion dominated escape of the VHE electrons from their production site, which determines the source extension in the electron cooling time. The diffusion coefficient in the Geminga-like scenario $D(100\text{TeV}) = 3.2 \times 10^{27} \text{ cm}^2/\text{s}$, which is significantly slower than the diffusion in the ISM (Abeysekara et al. 2017; Linden et al. 2017). The diffusion length and thus radius of a cooling dominated leptonic source is $r = \sqrt{2Dt_{\text{cool}}}$, and therefore $r_{\text{LHAASO,100TeV}} \approx 27\text{ pc}$, which is a size of a typical TeV halo object (Sudoh et al. 2019) and requires distance to the source $d > 6\text{kpc}$ in order not to exceed the LHAASO extension UL. We note that $r_{\text{LHAASO,100TeV}}$ only holds if the pulsar is older than t_{cool} . A comparison with the sample of known TeV PWNe shows that characteristic pulsar age for sources with such extension tends to be $\tau_c > 10\text{ kyr}$ (H. E. S. S. Collaboration et al. 2018a), which also meets expectations for the typical age of TeV halos $\sim 10^1 - 10^2 \text{ kyr}$ (Sudoh et al. 2019).

As noted above, the strong limit on $B \lesssim 1.2 \mu\text{G}$ only holds if the X-ray emitting region is relatively compact compared to the LHAASO upper limits on the TeV extension. Therefore, we also test the leptonic scenario of emission for magnetic field on the level of Galactic background, i.e. $B \approx 3 \mu\text{G}$. In such a case, cooling time of the cutoff energy electrons is no longer dominated by IC emission, and one has to take into account also synchrotron cooling time, given by

$$t_{\text{syn,yr}} \approx 1.3 \times 10^7 E_{\text{e,TeV}}^{-1} B_{\mu\text{G}}^{-2} \quad (4)$$

(Hinton & Hofmann 2009). The total cooling time is then $t_{\text{cool}} = (1/t_{\text{IC}} + 1/t_{\text{syn}})^{-1} \approx 10\text{ kyr}$, which leads to the total energy released by the tentative pulsar in the range of $E \approx 3 \times 10^{46} - 3 \times 10^{48} \text{ erg}$. The physical extension of the TeV halo following Geminga-like scenario for a pulsar older than t_{cool} is then $r_{\text{LHAASO,100TeV}} \approx 15\text{ pc}$, which is still consistent with the TeV halo hypothesis. LHAASO extension UL in this case require distance to the source $d > 3\text{kpc}$, which would prefer \dot{E} on the higher end of allowed pulsar spin-down powers constrained by the GeV emission. Such a powerful pulsar would still be able to provide the relativistic electrons with enough energy for any source distance in the Galaxy.

We also note that there is an unidentified point-like radio source NVSS 210803+515255 (Condon et al. 1998), or WENSS B2106.4+5140 (de Bruyn et al. 2000), well within the 95% error ellipse of the source 4FGL J2108.0+5155. We did not use the radio flux points to further constrain HE emission of the tentative pulsar as it in general does not follow PL from radio to sub-GeV.

3.2 Hadronic scenario of emission

The absence of an X-ray counterpart supports a hadronic emission mechanism, where UHE gamma rays are produced through inelastic collisions of hadronic relativistic CR with thermal protons, followed by π^0 decay (see Kafexhiu et al. (2014)). There is an open stellar cluster, Kronberger 80, and an open cluster candidate, Kronberger 82 (Kronberger et al. 2006), in the close vicinity of LHAASO J2108+5157. These open clusters may

potentially act as sources of accelerated PeV protons, as young massive stars seem to contribute significantly to the Galactic CR (Aharonian et al. 2019). The interaction of the PeV protons with ambient gas leads to gamma-ray emission via π^0 decay, and thus may be responsible for the observed emission of LHAASO J2108+5157, which is spatially coincident with two relatively dense molecular clouds. However, the 95% confidence interval for the distance to Kronberger 80 derived from Gaia DR2 data is 7.9-13.7 kpc (Cantat-Gaudin & Anders 2020), which puts the mutual distance of the cluster and the farther cloud ($d_1 \approx 3.1$ kpc) at more than 4.8 kpc, excluding the possibility of protons accelerated in this stellar cluster interacting with both molecular clouds. Note that the same can be concluded for the previously reported distance of Kronberger 80, which is 4.98 kpc (Kharchenko et al. 2016). The distance to Kronberger 82, however, remains unknown and one cannot exclude that this open cluster is close to one of those molecular clouds. Another source of CR protons are SNRs, proven to accelerate protons emitting gamma rays of multi-TeV energies (Ackermann et al. 2013), which diffuse away from their acceleration sites and interact with interstellar medium and molecular clouds as observed in several cases (i.e. W28 (Aharonian et al. 2008) or IC443 (Albert et al. 2007)).

Assuming a π^0 decay dominated origin of the UHE emission, we used `jetset` v1.2.1¹⁰ (Tramacere et al. 2009, 2011; Tramacere 2020) package and its implemented frequentist fitting routines (based on `iminuit`) to fit the LST-1 and LHAASO fluxes with a model assuming injected proton distribution in form of exponential cut-off power law. The hadronic pp model implemented in `jetset` is based on the parametrization of Kelner et al. (2006), and takes into account the γ -ray emission from π^0 decay, radiation (synchrotron, IC, and bremsstrahlung) from the secondaries (evolved to equilibrium) of charged pions and neutrinos. This means that, for each step of the minimization, secondaries pairs are evolved to the equilibrium, taking into account synchrotron radiation and escape time scales. Table 5 shows the best-fit model parameters shown in Figure 8 for both molecular clouds in the direction of the source, where the distances, total number densities of target protons, and sizes of the emitting regions were fixed on the values reported in Section 2.4. The best models yield cut-off energy of relativistic protons $E_{c,1,2} = 213 \pm 31$ TeV consistently for both molecular clouds. The total required energy of all relativistic protons interacting with molecular cloud is $E_{T,1} = 8.4 \times 10^{46}$ erg and $E_{T,2} = 1.7 \times 10^{46}$ erg, assuming interaction of protons with farther and closer molecular cloud, respectively. That is well below an energy content of CR protons interacting with molecular clouds in the vicinity of W28 and IC 443, which is 1–10 % of a typical SN total energy $E_{SN} \approx 10^{51}$ erg (Ackermann et al. 2013; Cui et al. 2018). Required spectral index of the proton distribution $\alpha_{1,2} = 0.5 \pm 0.3$ tends to be very hard compared to the standard DSA theory (e.g. Bell 1978). However, hard spectral indices are expected in the non-linear regime of efficient DSA (Berezhko & Ellison 1999; Malkov & Drury 2001; Amato & Blasi 2006). Hard proton spectral index can be also expected if VHE protons can only leave the acceleration region and interact with the clouds (Gabici & Aharonian 2007). In addition, Gabici & Aharonian (2014) showed that a hard GeV proton spectrum can be produced if gas clumps are present within the shell of a SNR. Alternatively, such a hard spectrum can be expected if the acceleration is dominated by stochastic processes in turbulent environments, such as the dense molecular clouds in the center of the Galaxy (e.g. Amano et al. 2011). Following the stochastic scenario in Amano et al. (2011), we can evaluate the expected value of E_c by equating the acceleration timescale to the dominant loss timescale. The acceleration timescale can be expressed as $\tau_{acc} \simeq 20$ yr $(\frac{\xi}{10})(\frac{B}{100\mu G})(\frac{n}{100 cm^{-3}})(\frac{E}{GeV})$ (Amano et al. 2011), where ξ is the scattering efficiency, that in the Bohm limit is ≈ 1 . The dominant cooling time, that for the protons is due to nuclear collisions, is given by $\tau_{loss-pp} \simeq 3.7 \times 10^5$ yr $(\frac{n}{100 cm^{-3}})^{-1}$ (Amano et al. 2011). Assuming the presence of a fast wind ($\gtrsim 100$ km s $^{-1}$), the escape time reads $\tau_{esc} \simeq 4.1 \times 10^5$ yr $(\frac{V_{wind}}{100 km s^{-1}})(\frac{R}{42 pc})$ (Amano et al. 2011). For values of $n \approx 100$, $R \gtrsim 1$ pc, and $V_{wind} \approx 100$ km s $^{-1}$, the dominant loss time is τ_{esc} , and imposing $\tau_{esc} = \tau_{acc}$, we obtain a value of $E_c > 100$ TeV, for $\xi \gtrsim 1$ and $B \gtrsim 3 \times 10^{-4}$ G, that is compatible with our best fit results. In Figure 8 we also show for reference the π^0 decay emission model with $\alpha = 2$ (fixed), proposed by Cao et al. (2021a), which we found to be ruled out by the *Fermi*-LAT and LST-1 ULs. In order not to violate the ULs, π^0 decay dominated emission models with soft $\alpha = 2$ would require very high minimum energy of the injected relativistic protons $E_{min} \approx 100$ TeV, which brings unavoidable theoretical challenges. The total neutrino flux resulting from $\pi^{+/-}$ decay is comparable with the gamma-ray flux in the TeV range (see Figure 8), which makes this source to be an interesting candidate for a follow-up analysis of data from a neutrino detector in this region. We note, however, that sensitivity of current neutrino detectors is about an order of magnitude lower than the predicted neutrino flux, and only future instruments will have a potential to definitively confirm/reject the hadronic emission hypothesis (e.g. Aartsen et al. 2019).

¹⁰<https://jetset.readthedocs.io/>

Parameter	Best fit value		Frozen
	Cloud 1	Cloud 2	
n [cm $^{-3}$]	115	240	True
d [kpc]	3.1	2.0	True
R [pc]	7.1	4.5	True
γ_{\min}	1.0	1.0	True
γ_{\max} [$\times 10^9$]	1.0	1.0	True
B [mG]	≤ 5.2	≤ 15.1	False
N [$\times 10^{-14}$ cm $^{-3}$]	1.1 ± 0.3	0.9 ± 0.2	False
γ_{cut} [$\times 10^5$]	2.3 ± 0.3	2.3 ± 0.3	False
α	0.5 ± 0.3	0.5 ± 0.3	False

Table 5: Best fit parameters of π^0 decay dominated VHE-UHE emission of LHAASO J2108+5157 for both molecular clouds in the direction of the source. The injected protons are assumed to be distributed according to an exponential cut-off power law with γ -factor in the range ($\gamma_{\min}, \gamma_{\max}$), cutoff at γ_{cut} , spectral index α , and total numeric density N .

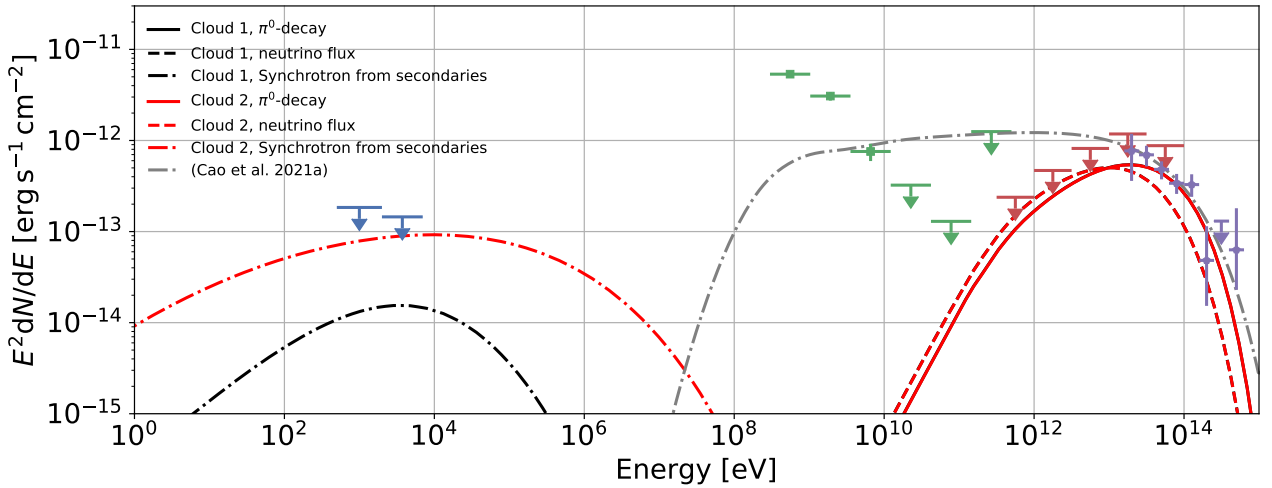


Figure 8: Multiwavelength SED of LHAASO J2108+5157 with hadronic models of emission. Observations with different instruments are represented by datapoints of different colours - *XMM-Newton* $r = 6'$ (blue), *Fermi-LAT* (green), LST-1 (red), LHAASO-KM2A (purple). The best fitting hadronic model of VHE-UHE emission (full line) has hard spectral index of the proton distribution $\alpha_{1,2} = 0.5 \pm 0.3$ for both clouds consistently. Dashed lines represent the total neutrino flux for both clouds. Black and red dash-dotted lines represent synchrotron emission of secondary particles for both clouds. Grey dash-dotted line represents π^0 decay emission model with $\alpha = 2$ shown for reference (Cao et al. 2021a).

The HE gamma-ray emission cannot be explained in a single component hadronic scenario together with VHE-UHE emission. Cao et al. (2021a) suggested that spectrum of the extended source 4FGL J2108.0+5155e may be associated with an old SNR, which usually features soft spectrum above 1 GeV (Acero et al. 2016; Li et al. 2021). Our dedicated analysis of *Fermi*-LAT data, however, shows that the Gaussian extended source assumption was not correct. If we fit the SED of 4FGL J2108.0+5155 in the *Fermi*-LAT energy band above 1 GeV with a single PL, it would provide a photon index $\Gamma = 3.2 \pm 0.2$, which in turns tends to be too soft compared to the observations of old SNRs interacting with dense molecular clouds (see Yuan et al. 2012).

While the hard UHE gamma-ray emission cannot be explained by interaction of the CR sea with the molecular clouds due to its soft spectrum of about $\alpha > 2.7$ in the outer parts of the Galaxy (Acero et al. 2016), one may argue that the CR sea can contribute significantly to the HE emission. Energy density of CR at Galactocentric radii > 8 kpc is $u_{\text{CR}}(E > 1 \text{ GeV}) \approx 0.5 \text{ eV cm}^{-3}$ (Yang et al. 2016), which is lower than observed in the Solar System. Considering the angular resolution of *Fermi*-LAT at 1 GeV, which is about 0.9° , UL on the radius of 4FGL J2108.0+5155 to still appear as a point-like source can be written as $R < d \tan(0.9^\circ)$. It results in rather weak limits on the proton energy density $u_{p,1}(E > 1 \text{ GeV}) > 0.14 \text{ eV cm}^{-3}$ and $u_{p,2}(E > 1 \text{ GeV}) > 0.10 \text{ eV cm}^{-3}$, for the farther and the closer molecular cloud, respectively, and hadronic origin of the HE emission cannot be therefore excluded.

4 Summary and conclusions

In this work, we present a multi-wavelength study of the unidentified UHE gamma-ray source LHAASO J2108+5157, which has not been found to be associated yet with any PWN, SNR or pulsar. Dedicated observations of the source with LST-1, yielding 49 hours of good quality data, resulted in a hint (2.2σ) of hard-spectrum emission at energies between 300 GeV and 100 TeV, which can be described with a single PL with photon index $\Gamma = 1.62 \pm 0.23$. Data analysis with selection cuts optimized for source detection show a possible excess (3.7σ) at energies $E > 3$ TeV. Even though a confirmed detection of the VHE emission would require deeper observation, the LST-1 data provide important constraints on the source emission in the TeV range.

The VHE-UHE gamma-ray emission can be well described with IC dominated emission of relativistic electrons with spectral index $\alpha = 1.5 \pm 0.4$ and cut-off energy $E_c = 100_{-30}^{+70}$ TeV, favouring the the PWN scenario. However, there is no sign of any X-ray source in 13.6 ks of dedicated observation with *XMM-Newton*, which puts strong constraints on the magnetic field in the emission region, $B < 1.2 \mu\text{G}$, if the X-ray emitting region is relatively compact compared to the extension ULs of the source in the TeV regime. Such a weak magnetic field can be expected for TeV-halo sources provided their extension compared to compact PWNe. Only detailed morphological study of the region with a high resolution instrument, such as the future completed CTA observatory, or a deeper X-ray observation can shed more light on the TeV-halo hypothesis.

The lack of detection of a pulsar associated with the UHE source presents another challenge for the TeV-halo scenario. Our dedicated analysis of the 12-years *Fermi*-LAT data allowed us to precisely determine the spectral properties of the HE source 4FGL J2108.0+5155, spatially consistent with LHAASO J2108+5157. The spectral analysis shows that the HE emission is compatible with the spectral properties of the population of known gamma-ray pulsars, characterized with soft spectra. Limits on the total energy released by the tentative pulsar, given by the luminosity of the source and relativistic electron cooling time, significantly exceed the total energy in relativistic electrons and it would therefore be able to power the VHE-UHE emission.

The presence of two molecular clouds in the direction of LHAASO J2108+5157 supports a hadronic scenario of emission, where the UHE gamma rays would be produced due to interaction of relativistic protons accelerated in a close stellar cluster or SNR with one of the two molecular clouds. In such scenario, X-ray ULs on synchrotron radiation of secondaries would allow for significantly higher levels of magnetic field in the source compared to the leptonic scenario of emission. We performed a detailed spectral modeling under the assumption of π^0 decay dominated emission, yielding a cut-off energy of the underlying relativistic protons of $E_{c,1,2} = 213 \pm 31$ TeV, for both clouds consistently. While the total energy in relativistic protons is low enough compared with the typical energy of SN explosion, the required spectral index is too hard ($\alpha_{1,2} = 0.5 \pm 0.3$) compared to the standard DSA, however, hard spectral indices are expected in the non-linear regime of efficient DSA. Such a hard spectrum can also be expected if the acceleration is dominated by stochastic acceleration processes in molecular clouds with turbulent magnetic field, or in the case when gas clumps are present in a SNR shell.

The HE gamma-ray emission in the hadronic scenario cannot be explained in a single component model together with VHE-UHE emission. While the old SNR scenario seems to be unlikely due to the very soft spectral index of the emission, the lower limit on the relativistic proton energy density is compatible with an interaction of the CR sea with the molecular clouds.

The total neutrino flux predicted in our model is comparable with the gamma-ray flux in the TeV range, which makes LHAASO J2108+5157 to be an interesting candidate for future neutrino experiments, sensitive enough to either confirm or reject the hadronic scenario of emission.

Author Contribution

M. Balbo: *Fermi*-LAT data analysis, paper drafting and edition; D. Eckert: *XMM-Newton* data analysis, paper drafting and edition; J. Juryšek: LST data analysis, paper drafting and edition, theoretical modelling, theoretical interpretation; A. Tramacere: theoretical modelling, theoretical interpretation; G. Pirola: LST analysis cross-check; R. Walter: project initiator & leadership, theoretical interpretation, XMM TOO. The rest of the authors have contributed in one or several of the following ways: design, construction, maintenance and operation of the instrument(s) used to acquire the data; preparation and/or evaluation of the observation proposals; data acquisition, processing, calibration and/or reduction; production of analysis tools and/or related Monte Carlo simulations; discussion and approval of the contents of the draft.

Acknowledgement

We gratefully acknowledge financial support from the following agencies and organisations:

Conselho Nacional de Desenvolvimento Científico e Tecnológico (CNPq), Fundação de Amparo à Pesquisa do Estado do Rio de Janeiro (FAPERJ), Fundação de Amparo à Pesquisa do Estado de São Paulo (FAPESP), Fundação de Apoio à Ciência, Tecnologia e Inovação do Paraná - Fundação Araucária, Ministry of Science, Technology, Innovations and Communications (MCTIC), Brasil; Ministry of Education and Science, National RI Roadmap Project DO1-153/28.08.2018, Bulgaria; Croatian Science Foundation, Rudjer Boskovic Institute, University of Osijek, University of Rijeka, University of Split, Faculty of Electrical Engineering, Mechanical Engineering and Naval Architecture, University of Zagreb, Faculty of Electrical Engineering and Computing, Croatia; Ministry of Education, Youth and Sports, MEYS LM2015046, LM2018105, LTT17006, EU/MEYS CZ.02.1.01/0.0/0.0/16_013/0001403, CZ.02.1.01/0.0/0.0/18_046/0016007 and CZ.02.1.01/0.0/0.0/16_019/0000754, Czech Republic; CNRS-IN2P3, France; Max Planck Society, German Bundesministerium für Bildung und Forschung (Verbundforschung / ErUM), Deutsche Forschungsgemeinschaft (SFBs 876 and 1491), Germany; Istituto Nazionale di Astrofisica (INAF), Istituto Nazionale di Fisica Nucleare (INFN), Italian Ministry for University and Research (MUR); ICRR, University of Tokyo, JSPS, MEXT, Japan; JST SPRING - JPMJSP2108; Narodowe Centrum Nauki, grant number 2019/34/E/ST9/00224, Poland; The Spanish groups acknowledge the Spanish Ministry of Science and Innovation and the Spanish Research State Agency (AEI) through the government budget lines PGE2021/28.06.000X.411.01, PGE2022/28.06.000X.411.01 and PGE2022/28.06.000X.711.04, and grants PGC2018-095512-B-I00, PID2019-104114RB-C31, PID2019-107847RB-C44, PID2019-104114RB-C32, PID2019-105510GB-C31, PID2019-104114RB-C33, PID2019-107847RB-C41, PID2019-107847RB-C43, PID2019-107988GB-C22; the “Centro de Excelencia Severo Ochoa” program through grants no. SEV-2017-0709, CEX2019-000920-S; the “Unidad de Excelencia María de Maeztu” program through grants no. CEX2019-000918-M, CEX2020-001058-M; the “Ramón y Cajal” program through grant RYC-2017-22665; the “Juan de la Cierva-Incorporación” program through grant no. IJC2019-040315-I. They also acknowledge the the “Programa Operativo” FEDER 2014-2020, Consejería de Economía y Conocimiento de la Junta de Andalucía (Ref. 1257737), PAIDI 2020 (Ref. P18-FR-1580) and Universidad de Jaén; “Programa Operativo de Crecimiento Inteligente” FEDER 2014-2020 (Ref. ESFRI-2017-IAC-12), Ministerio de Ciencia e Innovación, 15% co-financed by Consejería de Economía, Industria, Comercio y Conocimiento del Gobierno de Canarias; the “CERCA” program of the Generalitat de Catalunya; and the European Union’s “Horizon 2020” GA:824064 and NextGenerationEU; We acknowledge the Ramon y Cajal program through grant RYC-2020-028639-I; State Secretariat for Education, Research and Innovation (SERI) and Swiss National Science Foundation (SNSF), Switzerland;

The research leading to these results has received funding from the European Union’s Seventh Framework Programme (FP7/2007-2013) under grant agreements No 262053 and No 317446. This project is receiving funding from the European Union’s Horizon 2020 research and innovation programs under agreement No 676134.

This research has made use of the observations obtained with *XMM-Newton*, an ESA science mission with instruments and contributions directly funded by ESA Member States and NASA. This research has made use of the SIMBAD database, operated at CDS, Strasbourg, France.

References

Aartsen, M. G., Ackermann, M., Adams, J., et al. 2019, arXiv e-prints, arXiv:1911.02561

Abdo, A. A., Ajello, M., Allafort, A., et al. 2013, *ApJS*, 208, 17

Abdo, A. A. et al. 2009, *Astrophys. J. Lett.*, 700, L127, [Erratum: *Astrophys.J.Lett.* 703, L185 (2009), Erratum: *Astrophys.J.* 703, L185 (2009)]

Abdollahi, S., Acero, F., Ackermann, M., et al. 2020, *ApJS*, 247, 33

Abdollahi, S., Acero, F., Ackermann, M., et al. 2022, *ApJ*, 933, 204

Abeysekara, A. U., Albert, A., Alfaro, R., et al. 2017, *Science*, 358, 911

Acero, F., Ackermann, M., Ajello, M., et al. 2015, *ApJS*, 218, 23

Acero, F., Ackermann, M., Ajello, M., et al. 2016, *The Astrophysical Journal Supplement Series*, 223, 26

Acero, F., Ackermann, M., Ajello, M., et al. 2016, *ApJS*, 224, 8

Ackermann, M., Ajello, M., Allafort, A., et al. 2013, *Science*, 339, 807

Aharonian, F., Akhperjanian, A. G., Bazer-Bachi, A. R., et al. 2008, *A&A*, 481, 401

Aharonian, F., Yang, R., & de Oña Wilhelmi, E. 2019, *Nature Astronomy*, 3, 561

Aharonian, F. A., Kelner, S. R., & Prosekin, A. Y. 2010, *PRD*, 82, 043002

Albert, A., Alfaro, R., Alvarez, C., et al. 2021, *ApJ*, 911, L27

Albert, J., Aliu, E., Anderhub, H., et al. 2007, *ApJ*, 664, L87

Amano, T., Torii, K., Hayakawa, T., & Fukui, Y. 2011, *PASJ*, 63, L63

Amato, E. & Blasi, P. 2006, *MNRAS*, 371, 1251

Ambrogi, L., Zanin, R., Casanova, S., et al. 2019, *A&A*, 623, A86

Amenomori, M., Bao, Y. W., Bi, X. J., et al. 2019, *Phys. Rev. Lett.*, 123, 051101

Ballet, J., Burnett, T. H., Digel, S. W., & Lott, B. 2020, arXiv e-prints, arXiv:2005.11208

Bamba, A., Anada, T., Dotani, T., et al. 2010, *The Astrophysical Journal*, 719, L116

Bell, A. R. 1978, *MNRAS*, 182, 147

Bell, A. R. 2013, *Astroparticle Physics*, 43, 56

Berezhko, E. G. & Ellison, D. C. 1999, *The Astrophysical Journal*, 526, 385

Berge, D., Funk, S., & Hinton, J. 2007, *A&A*, 466, 1219

Bolatto, A. D., Wolfire, M., & Leroy, A. K. 2013, *ARA&A*, 51, 207

Breuhaus, M., Hahn, J., Romoli, C., et al. 2021, *ApJ*, 908, L49

Breuhaus, M., Reville, B., & Hinton, J. A. 2022, *A&A*, 660, A8

Cantat-Gaudin, T. & Anders, F. 2020, *A&A*, 633, A99

Cao, Z., Aharonian, F., An, Q., et al. 2021a, *ApJ*, 919, L22

Cao, Z., Aharonian, F. A., An, Q., et al. 2021b, *Nature*, 594, 33

Condon, J. J., Cotton, W. D., Greisen, E. W., et al. 1998, *AJ*, 115, 1693

CTA Consortium, Acharya, B. S., Agudo, I., et al. 2019, *Science with the Cherenkov Telescope Array* (World Scientific Publishing Co. Pte. Ltd.)

Cui, Y., Yeung, P. K. H., Tam, P. H. T., & Pühlhofer, G. 2018, *ApJ*, 860, 69

Dame, T. M., Hartmann, D., & Thaddeus, P. 2001, *ApJ*, 547, 792

de Bruyn, G., Miley, G., Rengelink, R., et al. 2000, *VizieR Online Data Catalog*, VIII/62

de Jager, O. C. & Harding, A. K. 1992, *ApJ*, 396, 161

de Naurois, M. 2021, *Universe*, 7, 421

de Oña Wilhelmi, E., López-Coto, R., Amato, E., & Aharonian, F. 2022, *ApJ*, 930, L2

Deil, C., Zanin, R., Lefaucheur, J., et al. 2017, in *International Cosmic Ray Conference*, Vol. 301, 35th International Cosmic Ray Conference (ICRC2017), 766

Dickey, J. M. & Lockman, F. J. 1990, *ARA&A*, 28, 215

Eckert, D., Ettori, S., Pointecouteau, E., et al. 2017, *Astronomische Nachrichten*, 338, 293

Eckert, D., Finoguenov, A., Ghirardini, V., et al. 2020, *The Open Journal of Astrophysics*, 3, 12

Emery, G., Alispach, C., Dalchenko, M., et al. 2021, *arXiv e-prints*, arXiv:2108.04550

Faherty, J., Walter, F. M., & Anderson, J. 2007, *Ap&SS*, 308, 225

Fermi-LAT collaboration, :, Abdollahi, S., et al. 2022, *arXiv e-prints*, arXiv:2201.11184

Fomin, V., Stepanian, A., Lamb, R., et al. 1994, *Astroparticle Physics*, 2, 137

Fruck, C. et al. 2022, *Mon. Not. Roy. Astron. Soc.*, 515, 4520

Gabici, S. & Aharonian, F. A. 2007, *ApJ*, 665, L131

Gabici, S. & Aharonian, F. A. 2014, *MNRAS*, 445, L70

Gabici, S., Evoli, C., Gaggero, D., et al. 2019, *International Journal of Modern Physics D*, 28, 1930022

Ghirardini, V., Eckert, D., Ettori, S., et al. 2019, *A&A*, 621, A41

H. E. S. S. Collaboration, Abdalla, H., Abramowski, A., et al. 2018a, *A&A*, 612, A2

H. E. S. S. Collaboration, Abdalla, H., Abramowski, A., et al. 2018b, *A&A*, 612, A5

H. E. S. S. Collaboration, Abdalla, H., Abramowski, A., et al. 2018c, *A&A*, 612, A1

HAWC Collaboration, Abeysekara, A. U., Albert, A., et al. 2019, *arXiv e-prints*, arXiv:1909.08609

HI4PI Collaboration, Ben Bekhti, N., Flöer, L., et al. 2016, *A&A*, 594, A116

Hillas, A. M. 1985, in International Cosmic Ray Conference, Vol. 3, 19th International Cosmic Ray Conference (ICRC19), Volume 3, 445

Hinton, J. A. & Hofmann, W. 2009, *ARA&A*, 47, 523

Jogler, T. & Funk, S. 2016, *ApJ*, 816, 100

Juryšek, J., Lyard, E., & Walter, R. 2021, arXiv e-prints, arXiv:2111.14478

Kafexhiu, E., Aharonian, F., Taylor, A. M., & Vila, G. S. 2014, *PRD*, 90, 123014

Kar, A. & Gupta, N. 2022, *The Astrophysical Journal*, 926, 110

Kargaltsev, O., Rangelov, B., & Pavlov, G. 2013, in *The Universe Evolution: Astrophysical and Nuclear Aspects*. Edited by I. Strakovsky and L. Blokhintsev. (Nova Science Publishers), 359–406

Kelner, S. R., Aharonian, F. A., & Bugayov, V. V. 2006, *PRD*, 74, 034018

Khangulyan, D., Aharonian, F. A., & Kelner, S. R. 2014, *ApJ*, 783, 100

Kharchenko, N. V., Piskunov, A. E., Schilbach, E., Röser, S., & Scholz, R. D. 2016, *A&A*, 585, A101

Kronberger, M., Teutsch, P., Alessi, B., et al. 2006, *A&A*, 447, 921

Leung, G. C. K., Takata, J., Ng, C. W., et al. 2014, *The Astrophysical Journal*, 797, L13

Li, J., Liu, R.-Y., de Oña Wilhelmi, E., et al. 2021, *ApJ*, 913, L33

Li, T. P. & Ma, Y. Q. 1983, *ApJ*, 272, 317

Linden, T., Auchettl, K., Bramante, J., et al. 2017, *PRD*, 96, 103016

Liu, R.-Y., Ge, C., Sun, X.-N., & Wang, X.-Y. 2019, *The Astrophysical Journal*, 875, 149

López-Coto, R., de Oña Wilhelmi, E., Aharonian, F., Amato, E., & Hinton, J. 2022, *Nature Astronomy*, 6, 199

Lopez-Coto, R., Vuillaume, T., Moralejo, A., et al. 2022, *cta-observatory/cta-lstchain*: v0.9.6 - 2022-04-13

López-Coto, R. et al. 2021, in *37th International Cosmic Ray Conference*

MAGIC Collaboration, Acciari, V. A., Ansoldi, S., et al. 2020, *A&A*, 643, L14

Malkov, M. A. & Drury, L. O. 2001, *Reports on Progress in Physics*, 64, 429

Manchester, R. N., Hobbs, G. B., Teoh, A., & Hobbs, M. 2005, *The Astronomical Journal*, 129, 1993

Martin, J., Torres, D. F., Cillis, A., & de Oña Wilhelmi, E. 2014, *MNRAS*, 443, 138

Mattana, F., Falanga, M., Götz, D., et al. 2009, *ApJ*, 694, 12

Mayer, M., Brucker, J., Holler, M., et al. 2012, arXiv e-prints, arXiv:1202.1455

Miville-Deschénes, M.-A., Murray, N., & Lee, E. J. 2017, *ApJ*, 834, 57

Moderski, R., Sikora, M., Coppi, P. S., & Aharonian, F. 2005, *MNRAS*, 363, 954

Pacini, F. & Salvati, M. 1973, *ApJ*, 186, 249

Popescu, C. C., Yang, R., Tuffs, R. J., et al. 2017, *MNRAS*, 470, 2539

Roman-Duval, J., Jackson, J. M., Heyer, M., et al. 2009, *ApJ*, 699, 1153

Russeil, D., Zavagno, A., Mège, P., et al. 2017, *A&A*, 601, L5

Saz Parkinson, P. M., Xu, H., Yu, P. L. H., et al. 2016, *ApJ*, 820, 8

Sudoh, T., Linden, T., & Beacom, J. F. 2019, PRD, 100, 043016

Taylor, A. R., Gibson, S. J., Peracaula, M., et al. 2003, AJ, 125, 3145

Tibet AS γ Collaboration, Amenomori, M., Bao, Y. W., et al. 2021, Nature Astronomy, 5, 460

Tramacere, A. 2020, JetSeT: Numerical modeling and SED fitting tool for relativistic jets, Astrophysics Source Code Library, record ascl:2009.001

Tramacere, A., Giommi, P., Perri, M., Verrecchia, F., & Tosti, G. 2009, A&A, 501, 879

Tramacere, A., Massaro, E., & Taylor, A. M. 2011, ApJ, 739, 66

Vannoni, G., Gabici, S., & Aharonian, F. A. 2009, A&A, 497, 17

Wood, M., Caputo, R., Charles, E., et al. 2017, in International Cosmic Ray Conference, Vol. 301, 35th International Cosmic Ray Conference (ICRC2017), 824

Yang, R., Aharonian, F., & Evoli, C. 2016, Phys. Rev. D, 93, 123007

Yuan, Q., Liu, S., & Bi, X. 2012, ApJ, 761, 133

Zabalza, V. 2015, in International Cosmic Ray Conference, Vol. 34, 34th International Cosmic Ray Conference (ICRC2015), 922

Zeng, H., Xin, Y., & Liu, S. 2019, ApJ, 874, 50

Zhang, L., Chen, S. B., & Fang, J. 2008, The Astrophysical Journal, 676, 1210

Zhu, B.-T., Zhang, L., & Fang, J. 2018, A&A, 609, A110

A 2D LST-1 analysis

We present here the results of a first attempt of building significance and excess sky maps.

So far, LST-1 does not have a background model that could be used for background counts predictions. Nevertheless, a tool¹¹ has been developed for the creation from real data of an acceptance model that can be used for radial corrections in Gammapy background models. In our case, the background method adopted for the 2D analysis is the *ring*-background technique: in this method the OFF region is defined as a ring around a trial source position, and used to provide a background estimate (Berge et al. (2007)). Differently from the *reflected-region*-background model, in which we use the same offset between the ON and OFF regions and the pointing direction, with this method the detector acceptance can not be assumed to be constant within the ring, since it covers areas with different offsets from the pointing position (Berge et al. (2007)).

As mentioned, the radial acceptance model (which assumes the instrument response to be symmetrical under rotations around the pointing direction) is extracted directly from the data set under analysis on a run-by-run basis and then projected onto the sky in order to evaluate the background for the whole data set (de Naurois (2021)). We excluded the three putative γ -ray sources (LHAASO J2108+5157, 4FGL J2108.0+5155 and HS), in order not to contaminate the acceptance (de Naurois (2021)). As expected, what we could noticed is that the background acceptance rapidly decreases with energy; on other hand, it does not significantly change with the offset from the center of the FoV at the high energies we are looking at, since showers from high-energy gamma rays have a larger Cherenkov photon density on the ground than the ones produced by low-energy gamma rays, and the telescope is triggered by showers with larger impact parameters and hence large angular offsets (Berge et al. (2007)). Finally, in order to take into account the acceptance dependence on the zenith angle variation across the FoV, we divided the sample into 4 zenith bins and stacked them together according to the average run zenith angle.

In Figure 9, the significance and excess maps show an excess of signal above 3 TeV up to significance values above 4σ in the proximity of LHAASO J2108+5157. The Gaussian fit over significance distribution for

¹¹https://github.com/mdebony/acceptance_modelisation/tree/main/acceptance_modelisation

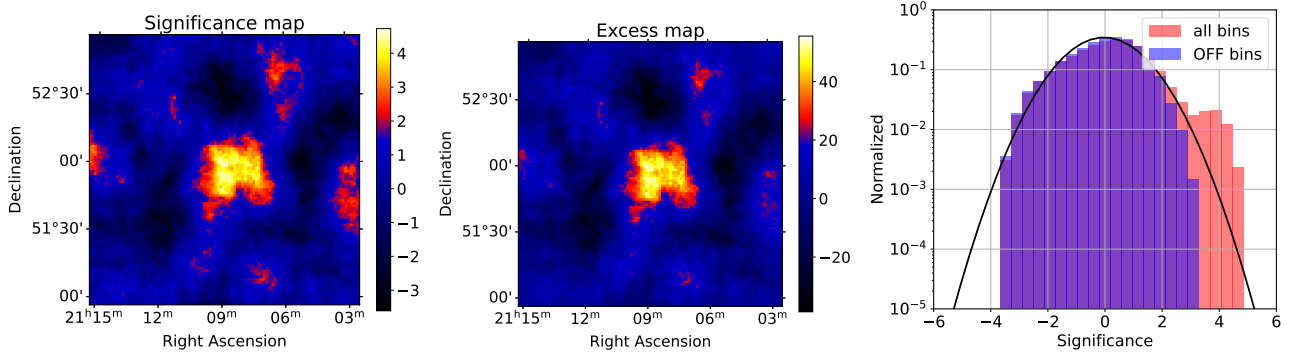


Figure 9: Statistical significance (*left*) and excess (*center*) maps in a region of $2^\circ \times 2^\circ$ around LHAASO J2108+5157, in the range of energy between 3 TeV and 100 TeV. The map was produced using `Gammapy` tool for the *ring*-background model: the OFF region is defined as a 0.3° radius ring, with a width of 0.3° , around a 0.2° radius circular ON region. The correlation radius for the building of the maps was fixed at 0.2° , accordingly to the value of the PSF (68% containment) in this range of energy, averaged for the different zenith bins used for the IRFs production. The same exclusion region adopted in the acceptance model building was used. *Right*: Significance distribution for the off bins (purple) and for all bins (pink). The black line represents Gaussian fit of the background, providing the mean value $\mu = -0.03$, and standard deviation $\sigma = 1.15$.

the off bins (see Figure 9) gives an average value consistent with 0, but the distribution is slightly asymmetric, meaning that the background modelling for our dataset is not perfect and can be improved.

LST-1 background modelling program is still under development, but it is already possible to use it to extract the the radial acceptance from real data and use it for radial corrections on the *ring*-background tool implemented in `gammapy`. Although the obtained background model has revealed not to be perfect for our dataset, we could find significance values in the skymap, reasonably consistent with that achieved through the 1D signal extraction above 3 TeV under the point-like source assumption (see Figure 1).